A stochastic, multiscale model of microwave backscatter from the ocean

William J. Plant

Applied Physics Laboratory, University of Washington, Seattle, Washington, USA

Received 11 April 2001; revised 15 August 2001; accepted 24 August 2001; published 6 September 2002.

[1] The conventional view of microwave backscatter from the ocean is based on composite surface and quasi-specular theories. In this view, backscatter at intermediate incidence angles is due to Bragg scattering from freely propagating short surface waves that are advected and modulated by longer waves. At small incidence angles the scattering process becomes quasi-specular, coming from small facets aligned normal to the incident waves. The transition between these two processes is said to occur at incidence angles of about 10° to 20°. In this paper we demonstrate that advances in scattering theory and in computing speed make it possible to improve this view. We show that recent scattering theories agree on the form of the backscatter for incidence angles below that where multiple scattering must be considered, i.e., below about 80°. This form involves the Kirchhoff integral multiplied by a coefficient dependent on dielectric constant and incidence angle. We avoid the higher-order calculations necessary in these theories to include the variable local incidence angle caused by surface wave slopes by applying them over restricted regions of the surface. We successively break the surface into regions from which the scatter comes from small-, intermediate-, and large-scale waves. We show that in this picture, scattering from small-scale waves is classic Bragg scattering and is very common while from large-scale waves it is classic quasi-specular scattering and is rarely important. For intermediate-scale waves we evaluate the Kirchhoff integral numerically; this type of scattering becomes increasingly important with increasing wind speed. For all scales but the large one we correct the incidence angle for the slopes of all longer waves as required by composite surface theory. On this picture the transition from Bragg scattering to Kirchhoff scattering occurs gradually in a manner that is dependent on incidence angle, azimuth angle, wind speed, and the surface wave spectrum. The model indicates that Bragg scattering is often viable to surprisingly low incidence angles at low wind speeds. The model is sensitive to the wave height variance spectrum over a wide range of wave numbers. We use two recently published forms of this spectrum to compare the predictions of the model to various data that have been collected over the incidence angles range from 0° to 50°. At 0° this model produces a better fit to Ku band data from the TOPEX altimeter than does quasi-specular theory and does so with no artificial "effective reflection coefficient." As the incidence angle increases, the model continues to show good agreement with data without an artificial division into "quasi-specular" and "Bragg" scattering. The advantage of this formulation over a quasi-specular one is demonstrated by comparing the two models with data on received power taken at 36 GHz for incidence angles between nadir and 30°. *INDEX TERMS:* 4275 Oceanography: General: Remote sensing and electromagnetic processes (0689); 4560 Oceanography: Physical: Surface waves and tides (1255); 6959 Radio Science: Radio oceanography; 6969 Radio Science: Remote sensing; *KEYWORDS:* ocean backscatter, model function, sea echo, composite surface theory, Bragg scattering, multiscale model

Citation: Plant, W. J., A stochastic, multiscale model of microwave backscatter from the ocean, *J. Geophys. Res.*, *107*(C9), 3120, doi:10.1029/2001JC000909, 2002.

1. Introduction

[2] Past attempts to develop a physical model of microwave backscatter from the ocean surface have relied on Bragg scattering, composite surface, and quasi-specular scattering theories [*Wright*, 1966, 1968; *Bass et al.*, 1968; *Barrick*, 1968; *Valenzuela*, 1978; *Durden and Vesecky*, 1985; *Plant*, 1986; *Donelan and Pierson*, 1987; *Apel*, 1994; *Romeiser et al.*, 1997; *Plant*, 1997]. Many advances have been made in recent years, however, in theories of microwave scattering from rough water surfaces [*Holliday*,

Copyright 2002 by the American Geophysical Union.
0148-0227/02/2001JC000909$09.00

1987; *Fung et al.*, 1992; *Voronovich*, 1985, 1994; *Thorsos and Broschat*, 1995]. These investigations clearly indicate that microwave backscatter from the ocean can more generally be described in terms of a Kirchhoff integral multiplied by a coefficient depending on incidence angle and dielectric constant. These results are similar to those used heuristically as a starting point by *Apel* [1994]. In his paper, however, Apel applied only the quasi-specular and Bragg scattering approximations to obtain his results from this starting point. Composite surface theory was not used by Apel since he did not consider tilting, modulation, and advection of the Bragg scatterers. All of the other attempts to physically describe microwave backscatter from the ocean have used Bragg scattering in combination with composite surface concepts, augmented by quasi-specular scattering at low angles. However, the effects of the long waves on the shorter ones have generally been included by integrating cross sections due to local Bragg scattering over the probability distribution of the long waves or by expanding in powers of the slope of the long wave. The recent theoretical advances when coupled with the speed of modern computers now make it possible to pursue another approach to this scattering problem. Individual realizations of the ocean surface can be obtained from one of the several forms of the surface wave height spectrum that have been suggested recently [*Donelan et al.*, 1985; *Plant*, 1986; *Banner*, 1990; *Elfouhaily et al.*, 1997]. Kirchhoff integral scattering can then be applied locally to backscatter from individual facets. Mean backscattering cross sections can be obtained by averaging those produced by the individual facets of the stochastically rough, long wave surface. This approach will be developed in this paper. The results will provide a method of calculating normalized radar cross sections of the sea over a range of incidence angles from nadir out to intermediate angles using a single method. This model will show that the Kirchhoff integral can be accurately approximated by Bragg scattering in many cases and will produce an estimate of the fraction of the total backscatter that can be described as Bragg scattering as a function of incidence angle and wind speed. Two different forms for the surface wave spectrum will be considered. We will leave to future work a description of the Doppler characteristics of the backscatter and of the nature of the return at high incidence angles where bound, tilted waves are important [*Plant*, 1997; *Plant et al.*, 1999a].

2. Overview

[3] The starting point of this model is a Kirchhoff integral formulation of backscatter similar to the one used by *Apel* [1994]. In the appendix, we show that both the Integral Expansion Method of *Fung et al.* [1992] and the small slope approximation of *Voronovich* [1994] yield the same expression for the normalized radar cross section of the sea for backscatter in terms of the Kirchhoff integral, although this expression is slightly different than the one postulated by Apel. We will divide the equation into parts corresponding to large, intermediate, and small wave heights, applying the expression to the latter two scales only over small facets of the surface. We believe that this is a better approach to applying the Kirchhoff formulation than applying it over all length scales on the ocean surface because the derivation of the formulation assumes stationarity and homogeneity, properties that the ocean surface does not have over a wide range of length scales. Recent studies have shown that the local incidence angle at a facet must be used to obtain correct scattering results [*Plant et al.*, 1999b]. Therefore, in applying this division of scales, we will let the local angle of incidence be determined by the nominal incidence angle and the slopes of all larger scales. By investigating backscatter from intermediate and small waves as functions of position on the large waves, we will be able to obtain the geometric (tilting) parts of modulation transfer functions. Hydrodynamic parts will be added separately by modulating the mean spectra of short and intermediate waves by the slopes of longer waves using our present understanding of modulation transfer functions. Furthermore, averaging the backscatter from large, intermediate and small-scale waves over many realizations of the long waves will yield average cross sections. For cases where the high frequency limit applies, these results should be comparable to quasi-specular theory; we will check this.

[4] Large wave heights correspond to long waves and we will artificially pick a cutoff wave number below which the waves will be considered large. From the spectrum in this low-wave number region, we will obtain realizations of the slopes of the large-scale surface for use in the small and intermediate scale calculations. The size of the large-scale facets over which this slope is held constant will be determined by the wavelength of the shortest wave that is considered to be large. Backscattering from these long waves will be approximated by quasi-specular scattering since its computation is faster than evaluating the Kirchhoff integral numerically. We will show that these long waves rarely contribute a significant amount of backscatter.

[5] We will depart a bit from the standard composite surface approach by considering an intermediate scale of surface waves whose lengths lie between those of long and short waves. We will determine the lengths of these waves based on the value of $k_o\sigma \cos\theta$, the product of the vertical wave number of the incident radiation times the RMS height of the surface. Intermediate wave heights will have intermediate values of this parameter and correspond to intermediate wave numbers. The Kirchhoff integral cannot be accurately approximated for these wave heights so we will solved the Kirchhoff integral numerically on each large-scale facet for which the Bragg wave number, $2k_o \sin\theta'$, where θ' is the local incidence angle, lies in the intermediate-scale range. Intermediate-scale backscatter will not come from large-scale facets that do not satisfy this condition; these are the facets that contribute to the stationary phase solution for the large scale that leads to quasi-specular scattering. In addition to adjusting the local incidence angle to allow for the local tilt of each large scale facet, we will allow the longer waves to modulate the mean intermediate-scale wave spectrum. Using the modulated spectra from this wave number range along with the large-scale slopes already calculated, we will then obtain realizations of slopes for use in the small-scale calculations. The size of these intermediate-scale facets will be determined by the wavelength of the smallest wave considered to be intermediate scale.

[6] Small wave heights correspond to high wave numbers and small values of $k_o\sigma \cos\theta$. The scattering theory reduces to Bragg scattering here. However, since the slopes of both the large and (modulated) intermediate scale waves are used

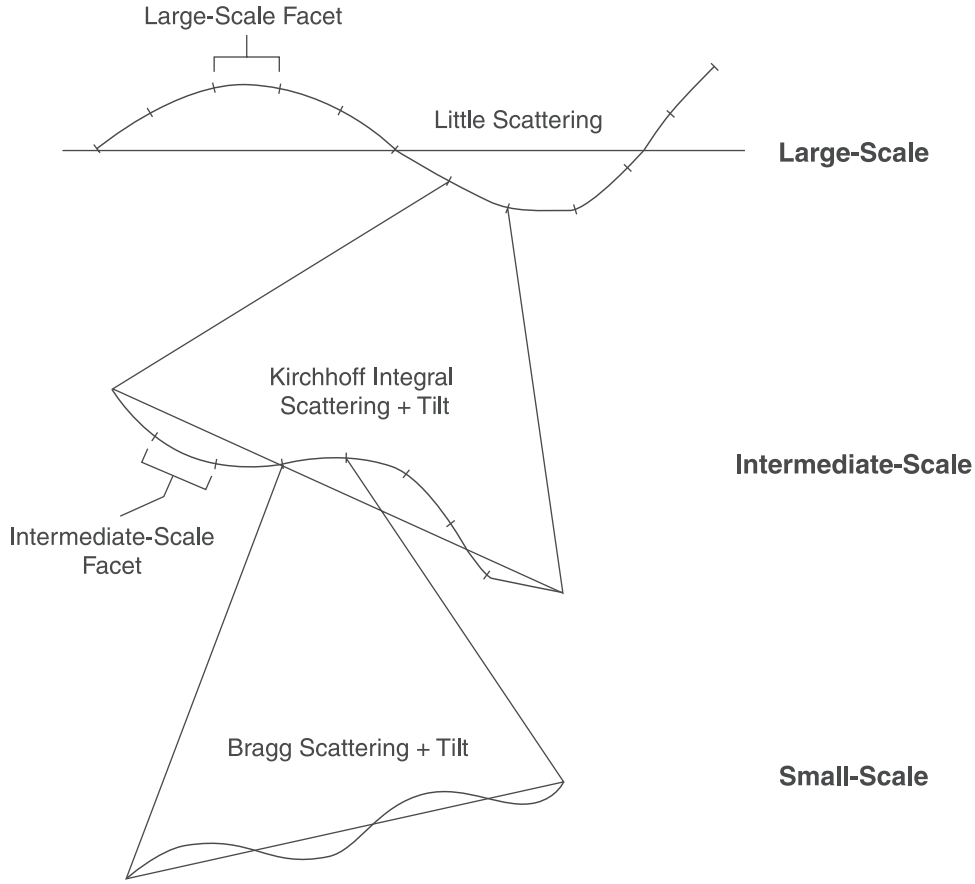

Figure 1. Schematic of the scattering model used in this paper.

in these calculations to change the local incidence angle of the Bragg scatterers, composite surface theory is obtained. Thus Bragg scattering is calculated from each intermediate-scale facet that is tilted by an amount that allows the Bragg wave number for the facet based on the local incidence angle to lie in the small-scale wave number range. Again no small-scale scatter comes from improperly oriented intermediate-scale facets.

[7] A. G. Voronovich (personal communication, 2000) has recently shown that results similar to this approach can be obtained by applying the Small Slope Approximation to second order. We believe that this technique would be difficult in general, however, and would obscure the physics of the processes affecting the backscatter. Additional justification for using local angles of incidence in our intermediate and small-scale wave calculations to take into account tilting by larger waves is also provided by work of Voronovich. His small-slope approximation for rough-surface scattering yields the scattered field when surface wave heights are input [*Voronovich*, 1994]. By separating these wave heights into large and small-scale parts, he has shown that composite surface theory, in which the local incidence angle varies with his large-scale slopes, can be obtained from his Small Slope Approximation for the scattering from the small-scale waves [*Voronovich*, 1996].

[8] A schematic of the approach being used here is given in Figure 1, which shows the division into large, intermediate, and small scales and the types of scattering coming from each. Scattering cross sections will be calculated as individual realizations of the cross sections of large, intermediate, and small scale waves. Averaging over many realizations of these cross section will produce total mean backscattering cross sections. We will only calculate like polarized cross sections in this paper.

[9] We mention in passing that if an infinite dielectric constant is used and no cross-slope admixture of VV return (see Section 3) is allowed, then the model developed here can also be applied to acoustic scattering from the sea surface. Acoustic scattering will be identical to HH polarized microwave scattering in this case.

3. Modeling Approach

[10] We show in Appendix A that both the Integral Expansion Method of *Fung et al.* [1992] and the Small-Slope Approximation of *Voronovich* [1994] yield the following equation for the normalized radar cross section of the sea for backscatter:

$$\sigma^o_{qp} = \frac{k_o^2}{\pi \cos^2\theta} |g_{qp}|^2 e^{-4k_o^2 \cos^2\theta\sigma^2} \int \left(e^{4k_o^2 \cos^2\theta\sigma^2 \rho(\xi,\zeta)} - 1 \right) \cdot e^{-i2k_o \sin\theta\xi} d\xi d\zeta \quad (1)$$

where ξ and ζ are lag distances in and perpendicular to the plane of incidence, k_o is the microwave number, θ is the incidence angle, q and p indicate polarization, and g_{qp} is given by

$$g_{vv} = \frac{(\epsilon - 1)[\epsilon(1 + \sin^2\theta) - \sin^2\theta]\cos^2\theta}{\left[\epsilon\cos\theta + \sqrt{\epsilon - \sin^2\theta}\right]^2} \quad (2)$$

for VV polarization and

$$g_{hh} = \frac{(\epsilon - 1)\cos^2\theta}{\left[\cos\theta + \sqrt{\epsilon - \sin^2\theta}\right]^2} \tag{3}$$

where ϵ is the relative dielectric constant. If the statistics are Gaussian, σ^2 is mean square surface wave height and ρ is the autocorrelation function of surface height. The "1" in the kernel of equation (1) removes the coherent part of the scattering. We add this part back into the equation for the remainder of this paper. We refer to the integral in equation (1) (with the "1" removed) as the Kirchhoff integral for historic reasons [*Beckmann and Spizzichino*, 1963]. We note that, while the Integral Expansion Method agrees with the Small-Slope Approximation in the case of backscatter, this has been shown not to be true for the more general bistatic case. In this case, the Integral Expansion Method does not reduce to small perturbation theory in the slightly rough surface approximation while the Small-Slope Approximation does [*Elfouhaily et al.*, 2001a].

[11] Equation (1) was derived under the assumptions that the surface waves were homogeneous and stationary, assumptions that are not valid for the sea surface on small time and space scales and are only marginally valid on intermediate scales if the longer waves are not held constant. To handle the inhomogeneous and nonstationary nature of the sea surface, we partition it into large, intermediate, and small scale waves and treat the larger scales deterministically in averages over smaller scales. Thus large-scale wave properties are kept constant in ensemble averages over intermediate and small-scale waves while large and intermediate-scale waves are held constant in ensemble averages over short waves. We assume that these filtered surfaces, large, intermediate, and small, each exhibit Gaussian statistics. If we make this partition of surface displacements into different scales and assume that they are phase decorrelated, we have

$$\sigma^2\rho = \sigma_l^2\rho_l + \sigma_i^2\rho_i + \sigma_s^2\rho_s \tag{4}$$

where the subscripts indicate large, intermediate, and small scales.

[12] Now consider the portion of the integral in equation (1) that covers small values of ξ and ζ. Over this range, ρ_l and ρ_i are nearly one so that factors containing them may be taken out of the integral to yield,

$$\sigma_{os} = \frac{k_o^2\,|g'_{qp}|^2}{\pi\cos^2\theta'}\int_{-s}^{s} e^{4k_0^2\cos^2\theta'\sigma_s^2(\rho_s(\xi,\zeta)-1)}e^{-i2k_o\sin\theta'_s\xi}d\xi d\zeta. \tag{5}$$

where the limits of integration correspond to the largest values of $|\xi|$ and $|\zeta|$ that we consider to be small.

[13] In equation (5), we have evaluated the cross section on a plane tilted because of the long and intermediate waves and have thus substituted θ' for θ where

$$\theta' = \theta - \gamma_l - \gamma_i \tag{6}$$

and γ_l and γ_i are the arctangents of the slopes of the long and intermediate waves in the plane of incidence. We also have added a prime to g_{qp} to indicate that long wave tilts out of the plane of incidence mix HH and VV polarizations [*Valenzuela*, 1968; *Plant*, 1990]. Thus we have

$$g'_{vv} \doteq g_{vv}(\theta') \tag{7}$$

while

$$g'_{hh} \doteq \cos^2\phi' g_{hh}(\theta') + \sin^2\phi' g_{vv}(\theta') \tag{8}$$

where

$$\phi' = \tan^{-1}\left(\frac{\alpha_l + \alpha_i}{\theta'}\right). \tag{9}$$

and α_l and α_i are the arctangents of the slope of the long and intermediate waves perpendicular to the plane of incidence. Note that the tilt of the plane of incidence also means that ρ_s is evaluated in a tilted reference frame.

[14] For these small-scale waves, the exponent containing the autocorrelation function in equation (5) is a small quantity and we may expand the exponential to yield,

$$e^{4k_0^2\cos^2\theta'\sigma_s^2(\rho_s-1)} \doteq 1 + 4k_o^2\cos^2\theta'\sigma_s^2(\rho_s - 1). \tag{10}$$

The spatially constant terms in this expression yield terms when substituted into equation (5) that are zero at small-scale wave numbers and therefore do not contribute to small-scale scattering. Substituting the other term into equation (5) and extending the limits of integration to infinity because ρ_s is negligible beyond these limit, we get

$$\sigma_{os} = 16\pi k_o^4\,|g'_{qp}|^2\,[F_s(2k_o\sin\theta'_s, 0) + F_s(-2k_o\sin\theta'_s, 0)] \tag{11}$$

where $F_s(k_x, k_y)$ is the one-sided, short wave spectrum defined such that its integral over all (k_x, k_y) is σ_s^2. The "x" subscripts refer to the axis in the plane of incidence while "y" indicates the perpendicular axis. Evaluating this equation for many realizations of large and intermediate-scale facets and averaging yields the composite surface theory result for the mean cross section due to small-scale waves.

[15] Turning now to the range of the integral in equation (1) corresponding to intermediate scales, we note that the short waves are well decorrelated on these scales so that $\rho_s = 0$. Furthermore, these scales are small enough so that we may let $\rho_l = 1$. Then, equation (1) reads for the intermediate scales,

$$\sigma_{oi} = \frac{k_o^2\,|g'_{qp}|^2}{\pi\cos^2\theta'}e^{-4k_o^2\cos^2\theta'\sigma_s^2}\int_{-i}^{i} e^{4k_o^2\cos^2\theta'\sigma_i^2(\rho_i(\xi,\zeta,\tau)-1)}e^{-i2k_o\sin\theta'\xi}d\xi d\zeta \tag{12}$$

where the integral is over all scales considered to be intermediate but excluding the small scales. θ' and g'_{qp} are the same as their small-scale counterparts except that α_i and γ_i are now omitted from equations (6) and (9). Since in this region, we cannot approximate the integral in equation (12) we will integrate it numerically. Then averaging over many

realizations of large-scale facets yields the mean cross section due to intermediate-scale waves.

[16] For the large-scale part of the cross section, we may make the standard high-frequency assumptions to solve equation (1). Thus we note that in the large-scale range of ξ and ζ, ρ_i and ρ_s are nearly zero so equation (1) can be written,

$$\sigma_{ol} = \frac{k_o^2 \, |g_{qp}|^2}{\pi \cos^2\theta} e^{-4k_o^2 \cos^2\theta(\sigma_i^2+\sigma_s^2)} \int_{-\infty}^{\infty} e^{4k_o^2 \cos^2\theta \sigma_l^2(\rho_l(\xi,\zeta)-1)} \cdot e^{-i2k_o \sin\theta\xi} d\xi d\zeta \tag{13}$$

We exclude the intermediate and smaller scales from this integral. In practice neither this omission nor the exclusion of small scales in equation (12) causes any real problem. Below, we will break the total spectrum of surface waves into parts corresponding to small, intermediate, and large scales. For each region the spectrum will be set to zero outside of some wave number range. Therefore, the correlation functions, which are digital Fourier transforms of the spectra will have a spatial resolution set by the inverse of the highest wave number included in the spectrum. This means that long wave correlation functions will contain no information on intermediate scales, and intermediate wave correlation functions will contain no information on small scales. The omitted parts of the integrals are subresolution.

[17] Ignoring, then, the part of the integration range that was omitted and following standard procedures of ensemble averaging and applying the Kirchhoff approximation [*Ulaby et al.*, 1982], it is straightforward to evaluate equation (13) to obtain

$$\sigma_{ol} = e^{-4k_o^2 \cos^2\theta(\sigma_i^2+\sigma_s^2)} \cdot \left(\frac{|R(0)|^2 \sec^4\theta}{2(S_{\xi\xi}S_{\zeta\zeta} - S_{\xi\zeta}^2)^{1/2}} \right) e^{\left(-\frac{\tan^2\theta(S_{\zeta\zeta}\sin^2\phi + S_{\xi\xi}\cos^2\phi - 2S_{\xi\zeta}\cos\phi\sin\phi)}{2(S_{\xi\xi}S_{\zeta\zeta} - S_{\xi\zeta}^2)} \right)} \tag{14}$$

where S_{ij} is the ensemble average of the product of large-scale slopes in the i and j directions. Without the leading exponential factor, this is the standard quasi-specular result [*Barrick*, 1968; *Hesany et al.*, 2000]. The large-scale cross section, σ_{ol} is easily shown to be a very small number for microwave frequencies and reasonable values of σ_s^2 and σ_i^2; we will give examples in section 6. Thus, in most cases the large-scale waves do not directly backscatter, exceptions being cases where the surface is nearly flat and the incidence angle is nearly zero.

[18] The two derivations of equation (1) used in Appendix A both implicitly assume that the antenna pattern is constant over decorrelation lengths on the surface. For intermediate waves, this is a very good assumption. It is possible, however, for our large scale surface to be perfectly flat. In this case the limits of integration in equation (13) will be determined by a windowing function caused by the antenna pattern that should really be included under the integral. Thus, the result in equation (14) should really be convolved with the Fourier transform this windowing function. This matters little, however, unless the surface is virtually flat and for that case, the value of σ_{ol} can be determined by a simple image method given in Appendix B. The result given implies that when the large-scale surface is flat but small and intermediate waves exist on the surface, σ_{ol} is approximately given by

$$\sigma_{ol} = e^{-4k_o^2 \cos^2\theta(\sigma_i^2+\sigma_i^2)} \left(\frac{8 \, |R(0)|^2}{\Phi_1^2} \right) e^{-8(\ln 2)\theta^2/\Phi_1^2} \tag{15}$$

where $R(0)$ is the (HH or VV) reflection coefficient at nadir and Φ_1 is the one-way, full, half-power antenna beam width. Thus the magnitude of σ_{ol} in this case depends on details of the antenna. This result can also be derived more tediously from equation (13) with a proper windowing function. As we will show below, this limit seldom gives appreciable backscatter except when small and intermediate waves are tiny and when the incidence angle is very nearly zero.

[19] In evaluating the overall mean cross section from the above equations, it is important to realize that because we used local incidence angles in equations (5) and (12), the integrals will be zero if $2\,k_o \sin\theta'$ falls outside of the small or intermediate scale wave number range, respectively. This means that if A_l is the total area, which is large in dimensions compared to the largest waves on the surface, then only in a part of this area $A_i < A_l$ will the large-scale facets that contain the intermediate-scale waves be oriented so that these waves backscatter. Similarly, for small-scale facets only a part $A_s < A_l$ of the total surface area will contribute to backscatter by small-scale waves. Thus the overall mean cross section is given by

$$\sigma_o = \sigma_{ol} + \left(\frac{A_i}{A_l} \right) \Sigma_{j=1}^{N_l} \sigma_{oi}^j + \left(\frac{A_s}{A_l} \right) \Sigma_{j=1}^{N_i} \sigma_{os}^j \tag{16}$$

where N_l and N_i are the number of large and intermediate-scale facets within the area A_l that have the proper orientations and the superscript "j" indicates the cross section of the jth facet. In cases where small-scale scattering is negligible, that is, where N_i is very small, we expect our result to be close to that given by quasi-specular theory. This agreement will depend on the accuracy of the stationary phase approximation invoked by quasi-specular theory to evaluate the integral in equation (12). In equation (16), σ_{ol}, σ_{oi}^j, and σ_{os}^j are all ensemble-averaged cross sections with larger scales held constant.

[20] We do not expect our results to be valid at very high incidence angles due to our neglect of multiple scattering and the probable dependence of σ_o on the exact surface morphology in this region. Thus we estimate the range of validity of the present model to be from incidence angles of 0° to about 80°. However, bound, tilted waves are known to contribute to the backscatter above about 50° [*Plant*, 1997]. At this time, the spectral form of these bound waves has not been determined, especially its angular spreading function. Thus such waves will not be included in the spectra to be discussed in the next section. For this reason, we will apply our model only out to incidence angles of 50° in this paper.

[21] In order to evaluate the equations given in this section, we need mean square heights and autocorrelation functions of the three different scales of waves along with slopes of intermediate and large-scale waves. We will obtain these quantities from forms of the mean ocean wave height

variance spectrum that have been developed by various workers in recent years. In the following section, we discuss these spectra.

4. Wave spectrum

[22] Evaluation of the wave height variance spectrum over the wide range of wave numbers required for this calculation is very difficult. This range will necessarily run from millimeter wavelengths to wavelengths on the order of 300 meters. No single technique is able to determine wave height variance spectral densities over the entire range due to resolution and dynamic range limitations. However, in recent years, several papers have been published which evaluate the required variance spectrum in various ranges using the results of measurements with wave gauge arrays, stereo photography, and microwave backscatter [*Donelan et al.*, 1985, hereinafter referred to as DHH; *Plant*, 1986; *Banner*, 1990]. We will utilize these results to obtain a form for the mean wave height variance spectrum over the required wide range of wave numbers. This will be the first spectral form we will consider in this paper. In addition to this, we will utilize the results of *Elfouhaily et al.* [1997] in our model. They have also attempted to synthesize the above results, and others, into a single, consistent form for the wave height variance spectrum over the whole range of wavelengths relevant on the ocean.

4.1. D Spectrum

[23] First let us consider the synthesis of DHH, Banner, and Plant into a single spectral form, which we will call the D spectrum. The appropriate form for the spectrum as a function of wave number and direction is a product of a wave number-dependent function and an angular spreading function. This is given by

$$F(k,\phi) = F(k,0)D(k,\phi) \tag{17}$$

where k is the wave number magnitude, and ϕ is its angle with respect to the direction toward which the wind blows, assumed to be $\phi = 0$. We will use the form for $D(k, \phi)$ obtained by DHH in their measurements of directional spectra on Lake Ontario using a wave gauge array. This form is given by

$$D(k,\phi) = \mathrm{sech}^2(\mathrm{B}\phi) \tag{18}$$

It is convenient to divide up the total wave number range of interest into that where gravity is the major restoring force, the gravity wave range, and that where surface tension also becomes important, the capillary wave range. In the gravity wave range, below $k = 30$ rad/m, we follow DHH and let B vary in various wave number ranges in the following manner

$$\mathrm{B_g} = \begin{cases} 1.22 & , \ k/k_p \le 0.31 \\ 2.61(k/kp)^{0.65} & , \ 0.31 < k/k_p \le 0.97 \\ 2.28(k/kp)^{-0.65} & , \ 0.97 < k/k_p \le 2.56 \\ 10^{[-0.4+0.8393\exp(-0.56\ln(k/kp))]} & , \ 2.56 < k/k_p \le 30/k_p \end{cases}$$

where k_p is the wave number at the peak spectral density in rad/m. Its determination will be discussed below. In the capillary wave range, above $k = 100$ rad/m, we take $\mathrm{B} = B_g = 1.24$ following *Donelan and Pierson* [1987]. Below we will discuss the transition between the two ranges.

[24] For wave numbers near the spectral peak, we converted the frequency spectrum given by DHH to wave number using the dispersion relation for gravity waves to obtain an expression for $F(k, 0)$. We modified this form, however, so that it corresponds to that given by *Banner* [1990] in the wave number range just above the spectral peak. Thus

$$F_g(k,0) = \left(\frac{\alpha}{k^4}\right)\exp\left\{-\left(\frac{k_p}{k}\right)^2\right\}G^H \tag{19}$$

DHH show that the parameters of this expression are different in their wind-wave tank than in the field. The two regimes may be differentiated on the basis of U/c_p where U is the neutral wind speed at 10 meters height and c_p is the phase speed of the wave with the maximum spectral density.

[25] Then, given the fetch x in meters and U in m/s, all parameters in equation (19) may be obtained as follows:

$$U/c_p = 11.6(xg/U^2)^{-0.23} \tag{20}$$

where g is gravitational acceleration in m/s^2,

$$\alpha = 0.001776(U/c_p)^{0.5} \tag{21}$$

$$k_p = g/c_p \tag{22}$$

$$G = \begin{cases} 1.7 & , \ U/c_p < 1 \\ 1.7 + 6.0\log(U/c_p) & , \ 1 \le U/c_p < 5 \\ 2.7(U/c_p)^{0.57} & , \ U/c_p \ge 5 \end{cases} \tag{23}$$

$$H = \exp\left[-\frac{(k/k_p)^{0.5} - 1)^2}{2s^2}\right] \tag{24}$$

where

$$s = \begin{cases} 0.08[1 + 4(U/c_p)^{-3}] & , \ U/c_p < 5 \\ 0.16 & , \ U/c_p \ge 5 \end{cases} \tag{25}$$

For $U/c_p < 5$, these expressions correspond to those given by DHH; above that, they provide a good fit to spectra measured in a wind-wave tank by *Plant* [1980]. Following Banner, we assume that these expressions are valid up to wave numbers of about 30 rad/m or wavelengths of about 20 cm.

[26] Finally, for the wavelength range where capillarity is important, *Plant* [1986] derived the following expression:

$$F_c(k,0) = \frac{Au_*^2}{c^2k^4} \tag{26}$$

where u_* is friction velocity and c is the phase speed of the wave of wave number k. Plant showed that this form fit microwave cross sections of the sea at intermediate incidence angles for microwavelengths of 2 and 6 cm if A was taken to be 0.002. However, if viscous dissipation is included in the growth rate used to derive this expression, it becomes

$$F_c(k,0) = \frac{Au_*^2}{c^2k^4} - 100A\nu k^{-3}/c \tag{27}$$

where ν is the kinematic viscosity of water. We use this expression for wave numbers above 100 rad/m.

[27] The phase speed, c of these very short waves is dependent on the wind speed. In order to include this effect, we use the equations of *Plant and Wright* [1980]. For waves propagating in the wind direction, these are,

$$c = \left[c_o^2 - \frac{\rho_a}{\rho_w}\left(\frac{(\pi u_*)^2}{3\kappa} + U_a^2\right)\right]^{1/2} + U_w \tag{28}$$

where

$$c_o^2 = g/k + Tk \tag{29}$$

$$U_a = U_s + \frac{u_*}{\kappa}\ln\left(\frac{z_o^a + z}{z_o^a}\right) \tag{30}$$

$$U_w = U_s - \left(\frac{\rho_a}{\rho_w}\right)^{1/2}\frac{u_*}{\kappa}\ln\left(\frac{z_o^w + z}{z_o^w}\right) \tag{31}$$

where T is the surface tension of water divided by its density, ρ_a and ρ_w are the densities of air and water, respectively, U_s is the surface drift speed, z_o^a and z_o^w are roughness lengths in air and water, respectively, and κ is von Karman's constant, taken here to be 0.4. In equation (28), U_a and U_w are evaluated at $z = 0.0044\ (2\pi)/k$. Plant and Wright showed that two different sets of assumptions for the combination (U_s, z_o^w) produced nearly the same phase speeds. These combinations are

$$\begin{aligned} U_s &= 0.38u_*^{0.7} \\ z_o^w &= z_o^a \end{aligned} \tag{32}$$

and

$$\begin{aligned} U_s &= 0.6u_* \\ z_o^w &= 2.5\times 10^{-5}m. \end{aligned} \tag{33}$$

We have chosen to use the latter combination in this work.

[28] In order to evaluate u_* and z_o^a, given U, we need to know the neutral drag coefficient, C_{dn}. If this is known, then

$$u_* = U\sqrt{C_{dn}} \tag{34}$$

and

$$z_o^a = 10\exp\left(-\kappa/\sqrt{C_{dn}}\right) \tag{35}$$

Colton et al. [1995] using measurements of Donelan similar to those reported by *Donelan* [1982] have shown that C_{dn} depends on both x and U. Therefore, we have taken C_{dn} to be given by

$$C_{dn} = \begin{cases} 0.001[0.8 + (0.04 + 0.07(U/cp - 0.83)/4.17)U] & ,\ 0.83 \le U/c_p < 5 \\ 0.001[0.8 + (0.04 + 0.07(U/cp - 0.83)/4.17)U] & ,\ 5 \le U/c_p < 9.17 \\ 0.001[0.8 + 0.04U] & ,\ \text{otherwise} \end{cases} \tag{36}$$

This form fits both the observations reported by Colton et al. and wave tank observations showing that C_{dn} returns to its long-fetch oceanic form at very short fetches [*Keller et al.*, 1992].

[29] The forms for $F(k, 0)$ in the two different wave number ranges, equations (19) and (26) do not come together smoothly at most wind speeds. Therefore we have inserted a transition region between them in the following manner. Let

$$a = 0.165 + 0.835\tanh[(k - 5\sqrt{U})/(25\sqrt{U})] \tag{37}$$

Then we let the overall spectrum be defined by

$$F(k,0) = F_g(k,0)(1-a) + F_c(k,0)a \tag{38}$$

and in the spreading function, D, we let

$$B = B_g(1-a) + 0.84a \tag{39}$$

Figure 2 shows $F(k, 0)$, $k^4F(k, 0)$, and $D(k, \phi)$ computed using this spectral form for various wind speeds and fetches of $x = 9.7\ U^2$ km. Note that this model is very similar to that of *Apel* [1994] except that he deals only with fully developed spectra and his spectra yield upwind slopes which exceed the limit of 0.06 proposed by *Plant* [1982] while the present model does not exceed that limit up to a wind speed of 25 m/s.

4.2. E Spectrum

[30] We turn now to the second spectral model used in this paper, that of *Elfouhaily et al.* [1997] (hereinafter referred to as ECKV). The basic approach is similar to that employed in the D spectrum in that the full spectrum is factored into a part dependent only on wave number and a part dependent also on direction. Now however, the wave number part is the integral over all directions rather than that in the wind direction:

$$F(k,\phi) = S(k)\Psi(k,\phi). \tag{40}$$

$S(k)$ is given by

$$S(k) = k^{-4}[B_l + B_h] \tag{41}$$

where B_l and B_h are curvature spectra at low and high frequencies, respectively. We use k^{-4} above rather than k^{-3} as ECKV did so that the mean squared height is obtained by integrating F over k dk dϕ.

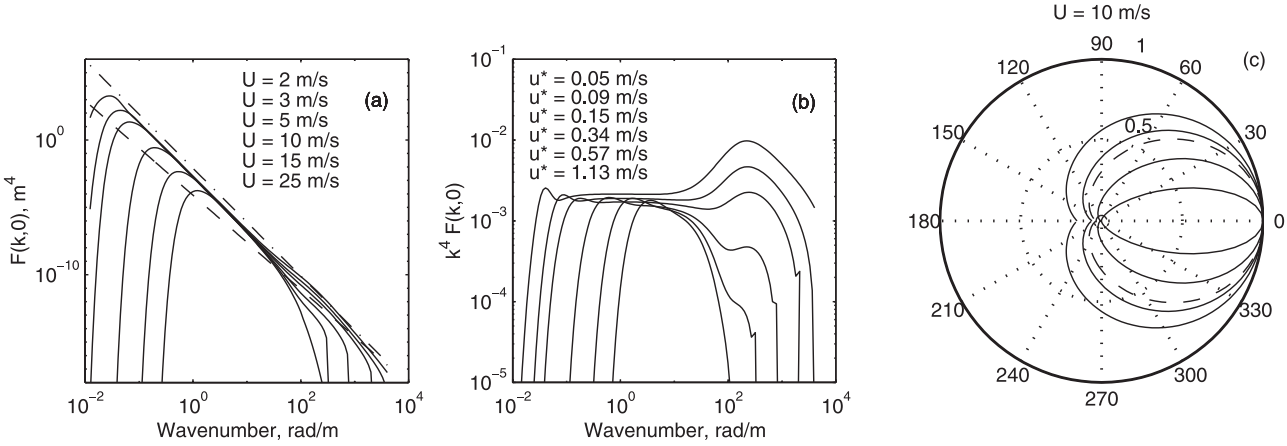

Figure 2. The D spectrum at various wind speeds and fetches of $9.7U^2$ km. (a) The wave height variance spectral density in the direction of the wind. The dash-dotted line in shows k^{-4}, while the dashed line is $k^{-3.5}$. (b) The curvature spectrum in the wind direction. (c) The angular part of the spectrum, $D(k, \phi)$. The solid lines show, in order of increasing loop size, k/k_p = 1, 3, 10, and 50, while the dashed line is k/k_p = 1000.

[31] The curvature spectra are given by ECKV as

$$B_l = 0.5\alpha_p\left(\frac{c_p}{c_o}\right)\exp\left\{-1.25\left(\frac{k_p}{k}\right)^2\right\}G^H\exp\left\{-\frac{U(\sqrt{k/k_p}-1)}{c_p\sqrt{10}}\right\} \tag{42}$$

where

$$\alpha_p = 0.006\sqrt{U/c_p} \tag{43}$$

and

$$B_h = 0.5\alpha_m\left(\frac{c_m}{c_o}\right)\exp\left\{-0.25\left[\left(\frac{k}{k_m}\right)-1\right]^2\right\} \tag{44}$$

where

$$\alpha_m = 0.014(u_*/c_m) \tag{45}$$

and c_m = 0.23 m/s is the value of c_o at $k = k_m$, the wave number of minimum phase speed, neglecting airflow.

[32] We have deviated from the paper of ECKV in two respects. First, we obtain u_* given U by using the drag coefficient given by equation (36). Second, we use a one-sided spectrum rather than a two-sided one. Thus we let Ψ have the shape first suggested by *Longuet-Higgins et al.* [1963]:

$$\Psi(k,\phi) = G(s)\cos(\phi/2)^{2s}. \tag{46}$$

For a one-sided spectrum, it is straightforward to relate s to $\Delta(k)$ given by ECKV. The relationship is

$$s = 1 - \ln\left(\frac{1-\Delta(k)}{1+\Delta(k)}\right)/\ln 2 \tag{47}$$

where

$$\Delta(k) = \tanh\left\{\frac{\ln 2}{4} + 4\left(\frac{c_o}{c_p}\right)^{2.5} + 0.13\left(\frac{u_*}{c_m}\right)\left(\frac{c_m}{co}\right)^{2.5}\right\}. \tag{48}$$

$G(s)$ is chosen so that the integral of $\Psi(k, \phi)$ over ϕ is one for all k.

[33] Figure 3 shows the E spectrum for various wind speeds and fetches of 9.7 U^2 km. Note that the spectrum is given in the figure in terms of $F(k, 0)$ and $D(k, \phi)$ so that it can be easily compared to the D spectrum.

5. Conversion of the Spectrum Into the Required Surface Quantities

[34] Given the spectrum $F(k, \phi)$, we integrate it over ϕ to get $F(k)$ and then determine the minimum k_2 such that

$$4k_o^2\cos^2\theta\int_{k_2}^{\infty}F(k)kdk \le 0.09. \tag{49}$$

This establishes the division between short and intermediate waves. We set the wave number dividing intermediate and large waves, k_1, by finding the smallest value of k_1 such that

$$4k_o^2\cos^2\theta\int_{k_1}^{k_2}F(k)kdk \le 9. \tag{50}$$

If $k_1 > k_2/6$, we set it to $k_2/6$. We then define small (F_s), intermediate (F_i), and large (F_l) scale spectra as follows:

$$\begin{aligned} F_s(\vec{k}) &= F(\vec{k}) \quad , \ k_2 \le k \\ F_i(\vec{k}) &= F(\vec{k}) \quad , \ k_1 \le k < k_2 \\ F_l(\vec{k}) &= F(\vec{k}) \ , \ 0 < k < k_1. \end{aligned} \tag{51}$$

and, where confusion may occur, will indicate wave numbers in the large, intermediate, and small-scale range by k_s, k_i, and k_l.

[35] In the large-scale region, we use F_l to calculate the large-scale slope $\vec{S}_l$ in and perpendicular to the plane of incidence. Let

$$a_l(\vec{k}) = e^{i\gamma(\vec{k})}\sqrt{F_l(\vec{k})}/dk \tag{52}$$

where $\gamma(\vec{k})$ is a random phase uniformly distributed between 0 and 2π. Also, assume that the antenna looks

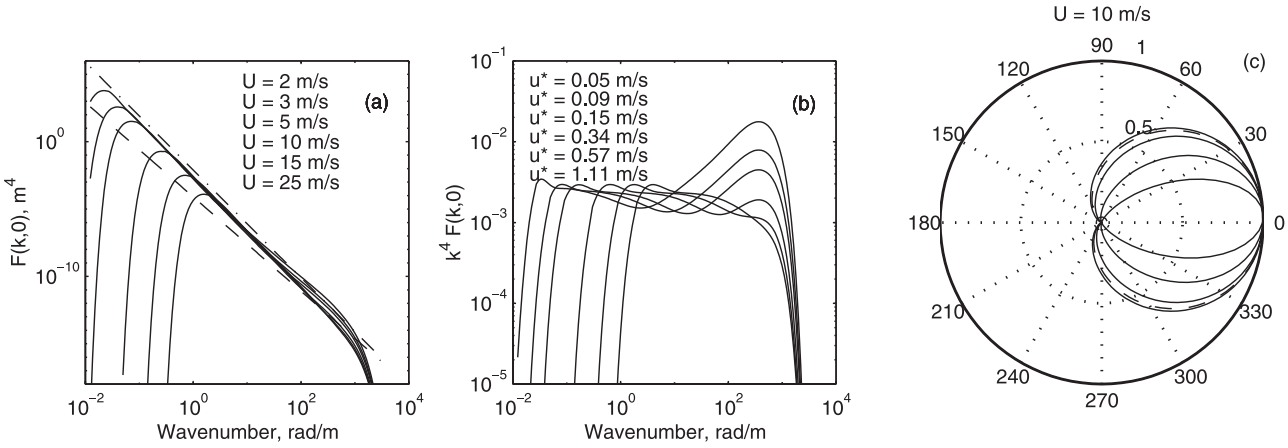

Figure 3. The E spectrum at various wind speeds and fetches of $9.7U^2$ km. (a) The wave height variance spectral density in the direction of the wind. The dash-dotted line in shows k^{-4}, while the dashed line is $k^{-3.5}$. (b) The curvature spectrum in the wind direction. (c) The angular part of the spectrum, $D(k, \phi)$. The solid lines show, in order of increasing loop size, k/k_p = 1, 3, 10, and 50, while the dashed line is k/k_p = 1000.

in the x direction, that y is the perpendicular horizontal direction and that z is vertical. Let $\vec{i_l}$, $\vec{j_l}$, and $\vec{k_l}$ be unit vectors in the horizontal look direction, in the perpendicular horizontal direction pointing left of $\vec{i_l}$, and in the vertical direction pointing upwards, respectively. Then,

$$\vec{S_l}(\vec{x}, t) = \int_0^{k_1} \left[\cos(\phi - \phi_a)\vec{i_l} + \sin(\phi - \phi_a)\vec{j_l} \right] ika_l(\vec{k}) d\vec{k} \quad (53)$$

where ϕ_a is the horizontal antenna look direction relative to the direction toward which the wind blows. We also need the mean square height of the large scale waves, given by

$$\sigma_l^2 = \int_0^{k_1} F_l(k) k dk \quad (54)$$

as well as various slope quantities for these waves:

$$\begin{aligned} S_{\xi\xi} &= \int_0^{k_1} k^2 \cos^2(\phi - \phi_a) F_l(\vec{k}) d\vec{k} \\ S_{\zeta\zeta} &= \int_0^{k_1} k^2 \sin^2(\phi - \phi_a) F_l(\vec{k}) d\vec{k} \\ S_{\xi\zeta} &= \int_0^{k_1} k^2 \sin(\phi - \phi_a) \cos(\phi - \phi_a) F_l(\vec{k}) d\vec{k}. \end{aligned} \quad (55)$$

[36] We must now calculate the hydrodynamic modulation of the intermediate-scale waves by the large ones. Thus the spectral density of the intermediate waves at a particular point in space after modulation by the large-scale waves is given by

$$F_{im}(\vec{k_i}; \vec{x}) = F_1 \left[1 + \int_0^{k_1} m(\vec{k_i}, \vec{k}) [ka(\vec{k})/\tanh kd] e^{-\vec{k}\cdot\vec{x}} d\vec{k} \right]. \quad (56)$$

[37] We use the expression of *Hara and Plant* [1994] for the hydrodynamic modulation transfer function, m:

$$m(\vec{k_i}, \vec{k}) = \left(-\left[\left(\frac{k_i}{F_i} \frac{\partial F_i}{\partial k_i} + \frac{c_{gi}}{c_i} - 1 \right) \cos^2(\phi_l - \phi_i) + \frac{1}{F_i} \frac{\partial F_i}{\partial \phi_i} \cdot \cos(\phi_l - \phi_i) \sin(\phi_l - \phi_i) \right] - \frac{i\beta m_\tau}{\omega_l} \frac{u_*}{F_i} \frac{\partial F_i}{\partial u_*} \right) \Big/ \left(1 - i\frac{\beta}{\omega_l} \right) \quad (57)$$

where m_τ is the shear stress modulation at the surface, $\omega_l = \sqrt{gk_l}$ is the long wave angular frequency, c_i and c_{gi} are the intrinsic phase and group speeds of the intermediate waves and the relaxation rate, β, is approximated by the magnitude of the growth rate given by [*Plant*, 1982]

$$\beta = \frac{0.04 u_*^2 k_i}{c_i} |\cos\phi_i|. \quad (58)$$

Hara and Plant determined m_τ from their microwave measurements looking into the wind at X band and intermediate incidence angles. A good fit to their measurements is given by

$$m_\tau = \left(\frac{30}{U} \right) e^{i\pi(15/U - 1)/8} \quad (59)$$

However, for reasons explained below, we let $m_\tau = 0$ in this model. The value of $F_{im}(\vec{k_i}, \vec{x})$ given by equation (56) is the spectrum of the intermediate waves to be used in the calculations below of intermediate wave quantities for fixed longwave parameters.

[38] For these intermediate-scale waves, we perform computations entirely analogous to those for long waves changing all "l" subscripts to "i", setting integration ranges from k_1 to k_2, and replacing F_l by F_{im}. Note that the use of F_{im} rather than F_i means that intermediate-scale heights and slopes will vary with position on the large-scale wave. Another difference now is that intermediate scale unit

vectors are rotated relative to the large-scale ones by the large-scale slopes. If we adopt the convention of rotating first in the plane of incidence then perpendicular to it, we have,

$$\begin{aligned}\vec{i}_i &= \cos\gamma_l\vec{i}_l + + \sin\gamma_l\vec{\kappa}_l\\ \vec{j}_i &= -\sin\alpha_l\vec{i}_l + \cos\alpha_l\vec{j}_l + \sin\alpha_l\cos\gamma_l\vec{\kappa}_l\\ \vec{\kappa}_i &= -\sin\gamma_l\cos\alpha_l\vec{i} - \sin\alpha_l\vec{j}_l + \cos\alpha_l\cos\gamma_l\vec{\kappa}_l.\end{aligned} \tag{60}$$

where $\vec{S}_1 = \tan\gamma_1\vec{i}_l + \tan\alpha_l\vec{j}_l$. In addition to the calculations of heights and slopes for the intermediate waves, we also must calculate the autocorrelation function, ρ_i. Since the mean square height of the intermediate waves after modulation by large-scale ones is given by

$$\sigma_{im}^2 = \int_{k_1}^{k_2} F_{im}\left(\vec{k}\right)d\vec{k}, \tag{61}$$

we may write the autocorrelation function as

$$\rho_{im}(\xi,\zeta) = \frac{1}{\sigma_i^2}\int_{k_1}^{k_2} F_{im}(\vec{k})e^{i\vec{k}\cdot\vec{\xi}}d\vec{k} \tag{62}$$

where $\vec{\xi} = \xi\,\vec{i}_i + \zeta\,\vec{j}_i$. Once again, note that the intermediate scale quantity, ρ_{im}, depends on location. This result for ρ_{im} may be substituted into the integrand of equation (12) for ρ_i, which can then be evaluated numerically.

[39] Small wave quantities are somewhat easier to deal with than the intermediate and large-scale ones since we need only know the spectrum. However, the spectrum is modulated by both the large and intermediate-scale waves. Thus the small-scale spectrum after modulation by the large-scale waves is

$$F_{sl}(\vec{k}_s;\vec{x}) = F_s\left[1 + \int_0^{k_1} m(\vec{k}_s,\vec{k})[ka_l(\vec{k})/\tanh kd]\,e^{i\vec{k}\cdot\vec{x}}d\vec{k}\right] \tag{63}$$

where m is given by equation (57) with "i" subscripts changed to "s". Now, these small-scale spectra are further modulated by the intermediate-scale waves:

$$F_{sm}(\vec{k}_s;\vec{x}) = F_{sl}\left[1 + \int_{k_1}^{k_2} m(\vec{k}_s,\vec{k})[ka_{im}(\vec{k})/\tanh kd]e^{i\vec{k}\cdot\vec{x}}d\vec{k}\right] \tag{64}$$

where

$$a_{im}(\vec{k}) = e^{i\gamma(\vec{k})}\sqrt{F_{im}(\vec{k})}/dk \tag{65}$$

[40] The modulated stress given by Hara and Plant was obtained by considering only modulation of short waves by long waves; the cascade process whereby long waves modulate intermediate waves which in turn modulate small scale waves was ignored. When we tried here to use equation (57) with m_τ given by equation (59) while also including this cascading modulation, we obtained modulations that were much too large, frequently yielding negative spectral densities for the small waves. This is the reason we have let $m_\tau = 0$ here. Substituting F_{sm} into equation (11) in place of F_s yields the part of the small wave cross section coming from that particular spatial location.

6. Comparison of Model Results With Data

[41] The model outlined above was coded in Matlab and run on a PC with a Pentium III 500 MHz processor and 128 MBytes of RAM. The code required approximately 5 min to obtain σ_o (VV) and σ_o $(H\,H)$ for a single wind speed, incidence angle, and azimuth angle. The scattering model was run using both the D and E spectral models. In addition, a variable wind speed was used in the D spectrum by computing the spectrum for various wind speeds within a small interval of variation, specified by the standard deviation of the wind speed (stdU). The procedure used is described in detail by *Plant* [2000]. The net result of including a variable wind speed in the D spectrum is to raise the spectral densities in the high wave number region for wind speeds below 5 m/s. Above this wind speed, variable winds have no effect on the calculations. Variable wind speeds have little effect on the E spectrum.

[42] Figure 4 compares the output of the model for a 0° incidence angle and 14 GHz microwave frequency with TOPEX/Poseiden altimeter data taken from *Hwang et al.* [1998]. The solid and dashed lines in Figure 4a are the result of evaluating the Kirchhof integral for the intermediate scale waves numerically using the D spectrum with no wind variability and using the E spectrum, respectively. The dotted(D spectrum) and dash-dotted (E spectrum) lines in the figure were obtained using the quasi-specular approximation for intermediate scale scattering. That is, equation (14) was evaluated with $\theta = \theta_i$ and $\sigma_i = 0$. At this incidence angle wind variability played little role in the predictions so no curves are shown for the D spectrum with wind variability. Obviously, the quasi-specular approximation does not fit the data as well as the complete numerical evaluation of the Kirchhof integral. Furthermore, these results indicate that cross sections at nadir are primarily due to intermediate scale waves that have been tilted by large scale waves so that they are effective scatterers at this incidence angle. Figure 4b shows the result of evaluating equation (14) for the large scale waves. Clearly these large scale waves contribute very little to the total backscatter at 0° incidence angle. Scattering from these waves drops rapidly with increasing incidence angle so the model shows that large scale waves virtually never contribute significantly to microwave backscatter from the ocean. As discussed in Section 3, the exception to this occurs when the sea is completely calm. For instance, if equation (15) is evaluated for a 0° incidence angle, a microwave frequency of 14 GHz, and an antenna beam width of 2°, the resulting large scale cross section linearly ranges between 36 dB and −39 dB for $\sigma_i + \sigma_s$ between 0 and 0.5 cm.

[43] Figure 5 compares model output with data collected from an airship by *Plant et al.* [1998] as a function of azimuth angle for various incidence angles. The data are for wind speeds of 2 and 8 m/s. The solid lines show that the D spectrum with no wind variability yields good fits to the 8 m/s data at all incidence angles and to the 2 m/s data at the 10° incidence angle. However, it begins to fall below the data at a 30° incidence angle and is so far below the data at a 50° incidence angle that it is below the bottom of the

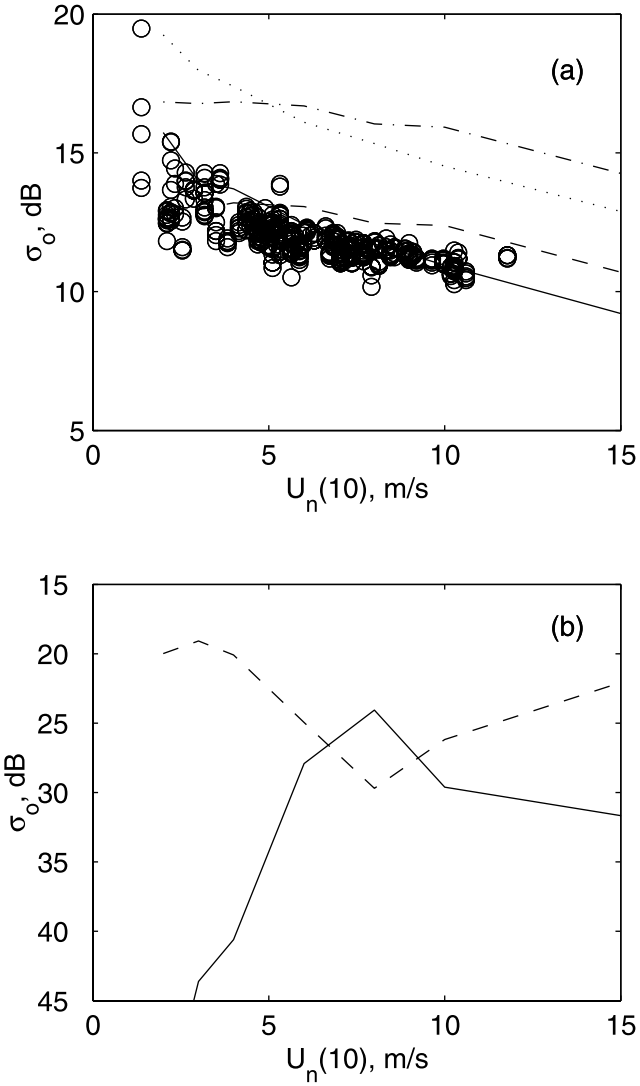

Figure 4. Cross sections at zero degrees incidence angle predicted by the model compared with those measured by the TOPEX/Poseiden altimeter. (a) Results of the full model. Solid line - D spectrum with numerical integration of the Kirchhof integral; dotted line - D spectrum with integral approximated by equation (14); dashed line - E spectrum with numerical integration of the Kirchhof integral; dash-dotted line - E spectrum with integral approximated by equation (14). Circles are data taken from *Hwang et al.* [1998]. (b) Results of quasi-specular scattering from only large-scale waves. Solid line - D spectrum; dashed line - E spectrum.

graph. This is in agreement with the results of *Plant* [2000] and suggests that the wind during the period of measurement was not perfectly constant at its mean value. Rather it exhibited variability so that the D spectrum with stdU = 1.5 m/s provides a better fit. Note that the fit is still not perfect as should be expected since data collection was spread over a period of about two weeks during which the wind variability could not be expected to remain constant. Note however, that this result provides a much better fit to the data than the results using the E spectrum that are shown as dashed lines. Obviously this spectral form does not produce sufficient roll off at low wind speeds. One obvious feature of these plots is that, except perhaps at 30° incidence, the angular dependence is only qualitatively correct. At 10° the model yields somewhat too much angular dependence while at 50° it does not produce enough. If the scattering model is correct, this suggests that neither of the spectral models has an angular spreading function that is correct.

[44] Figure 6 shows model predictions and data from *Plant et al.* [1998] for azimuthally averaged cross sections versus wind speed at three different incidence angles. The fit of all predictions to the data at the 10° incidence angle is rather good. This also applies to the other incidence angles at wind speeds above about 6 m/s, except perhaps for the predictions using the D spectrum at a 50° incidence angle and HH polarization. In this region the E spectrum seems to yield better results. Below wind speeds of about 6 m/s, the E spectrum yields values that are too high at the higher two incidence angles while the fit of the D spectrum to the data depends on wind variability, as usual.

[45] In order to check predictions of the model at various microwave frequencies, we ran the model for a range of frequencies from 1.2 to 17.25 GHz at three different incidence angles at a 10 m/s wind speed and compared its predictions with data from *Unal et al.* [1991] and with the CMOD4 and NSCAT2 scatterometer model functions. The results are shown in Figures 7–9. In all these figures the solid and dashed lines show results using the D spectrum at VV and HH polarizations, respectively. Dash-dotted and dotted lines are results using the E spectrum at VV and HH polarizations, respectively. Figure 7 shows data, scatterometer model function values, and model predictions for the azimuthally averaged cross section at various microwave frequencies. The model predictions are generally somewhat below the data of Unal et al. but closer to the values obtained from the scatterometer model functions. The ratio of VV to HH cross sections predicted by the model at a 45° incidence angle seems to be larger than either the data of Unal et al. or those given by the NSCAT2 model function. This is a common feature of Bragg/composite surface scattering models. A possible explanation for this discrepancy in terms of bound, tilted Bragg waves has been suggested by *Plant* [1997]. We feel that the nature of these waves is not sufficiently well understood to include in this model at the present time but will attempt to incorporate them in the future. Figure 8 compares upwind/downwind ratios of the measured and modeled cross sections for the two polarizations. Both data and model indicate that this ratio is often smaller than one at a 20° incidence angle. Predictions of the model using the E spectrum yield this result more often that those using the D spectrum. At the highest incidence angle, model predictions of this ratio are somewhat lower than the data, indicating that modulation of the short waves is perhaps not being accurately modeled. Finally, Figure 9 compares measured and modeled upwind/crosswind ratios of the cross sections for the two polarizations. Fits of the model predictions to the data are reasonably good except perhaps a the 45° incidence angle for the lower microwave frequencies. Also, the E spectrum produces a much worse fit to the data at 20° incidence than does the D spectrum. These results show that the model presented here when combined with accurate data can provide a sensitive means of checking our knowledge of

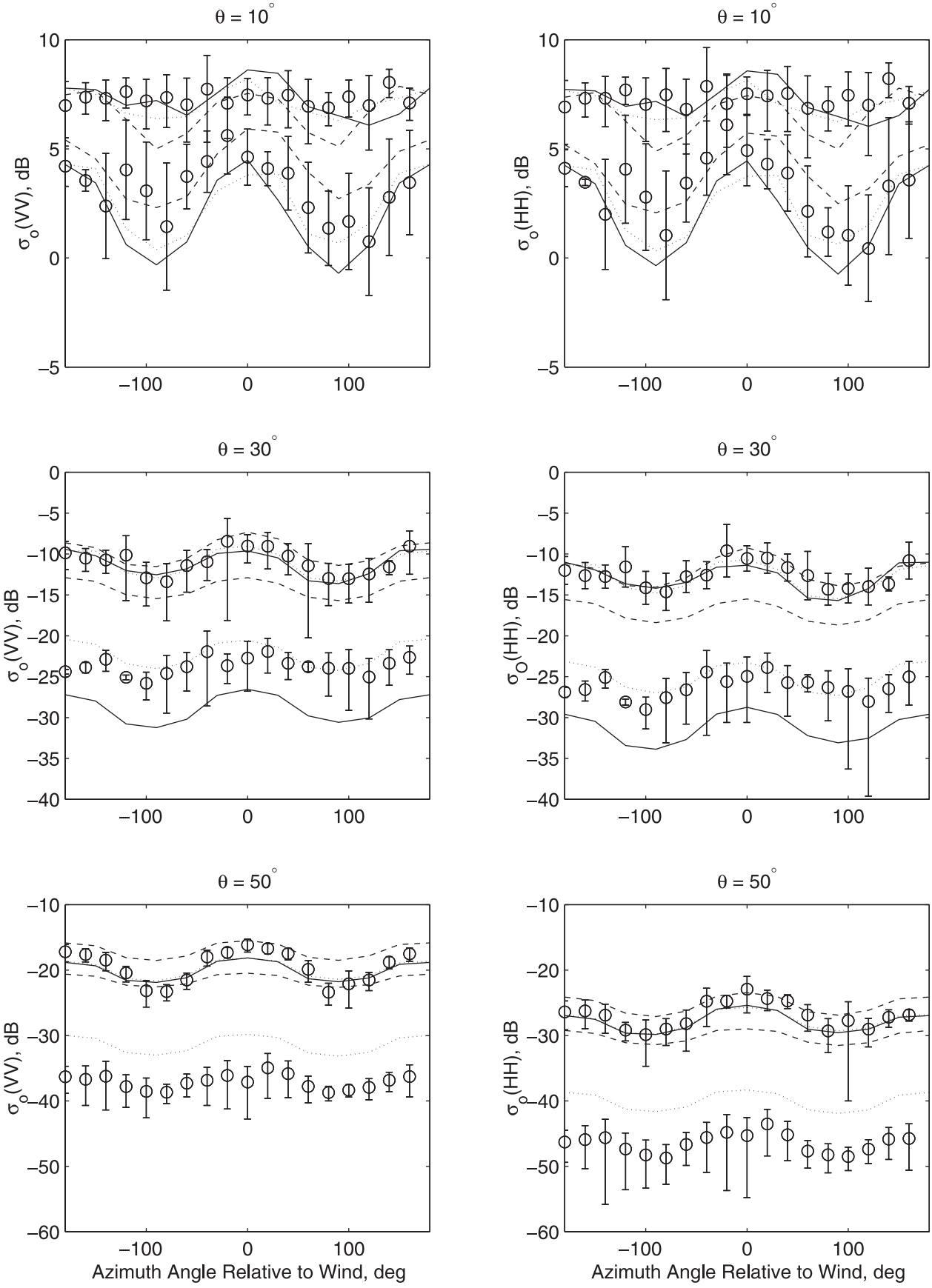
θ = 10°
θ = 10°
θ = 30°
θ = 30°
θ = 50°
θ = 50°
σo(VV), dB
σo(HH), dB
Azimuth Angle Relative to Wind, deg
Azimuth Angle Relative to Wind, deg

the spectrum and interactions of surface waves as well as the accuracy of the scattering model. Iteration of improvements in the scattering model and in our knowledge of surface waves should lead to a convergence of the modeled results with the data.

[46] A large set of data is available at 36 GHz as a result of many years operation of the Scanning Radar Altimeter (SRA) [*Walsh et al.*, 1998]. Unfortunately, these data are not absolutely calibrated to yield a normalized radar cross section of the sea surface. They do clearly show the dependence of the received power on incidence angles near nadir, however; such data have been used to infer the mean square slope of the sea surface. In Figure 10, we compare data given by *Banner et al.* [1999] (See their Figure 12) with the results of the present model using the D spectrum and with quasi-specular theory using the mean squared slope deduced by Banner et al. We have converted their measurements to normalized radar cross section in dB and forced them to fit the results of the present model at nadir. Using the radar equation, it is straightforward to show that the relationship between the logarithm of received power, $\ln(P_r)$, given by Banner et al. and σ_o in dB is

$$\sigma_o(dB) = C + [\ln(P_r) - \ln(A_l \cos^4\theta)]/0.23 \qquad (66)$$

where C is a constant, depending on the system. The total area A_l is pulse limited well off nadir and beam limited near nadir. Thus we let A_l be

$$A_l = \min\left(\frac{\pi\Phi^2 h^2}{4\cos^3\theta}, \frac{\sqrt{\pi}\Phi h \rho_r}{2\cos\theta\sin\theta}\right) \qquad (67)$$

where Φ is beam width (1°), h is altitude (40 m), and ρ_r is range resolution (15 cm). Comparisons are shown for wind speeds of 6.8 m/s and 15.4 m/s for upwind/downwind looks and for a wind speed of 15.4 m/s for a cross wind look. (Note that flight directions are given in Figure 12 of Banner et al., not antenna look directions.) Data from the present model are shown for HH and VV polarization as the symbols in Figure 11. Original data of Banner et al (VV polarized) are shown as the dashed line while data converted to σ_o are shown as dash-dotted lines. Quasi-specular predictions for the mean square slopes found by Banner et al., are shown as solid lines. The data fit both models very well out to incidence angles of about 12° (θ^2 = 0.044 radians^2). Mean square slopes given by Banner et al., which they obtained from quasi-specular theory over this range, agree well with mean square slopes given by the D spectrum for long and intermediate-scale waves. Values are compared in Table 1. Beyond 12° incidence, the quasi-specular predictions fall farther below the data than does the present model since quasi-specular theory does not make the transition to Bragg scattering as the present model does.

[47] As mentioned earlier, the present model makes the transition from quasi-specular, or Kirchhof integral, scattering to Bragg scattering in a natural and gradual manner. This is illustrated in Figure 11 for using the two different spectral forms. All parts of the figure display the fraction of the azimuthally averaged, VV polarized cross section that can be considered to be Bragg scattering as a function of wind speed and for incidence angles of 0°, 10°, 20°, and 35°. Figure 11a shows this fraction as predicted by the model using the D spectrum and no wind variability. Figure 11b is the same but with a standard deviation of wind speed of 1.5 m/s. Finally, Figure 11c shows the result of using the E spectrum in the model. Perhaps the most surprising aspect of these results is the fact that backscatter from the sea surface can often be considered to be Bragg scattering at low wind speeds even at quite low incidence angles. Thus at an incidence angle of 10°, between 40 and 70% of the backscatter at a 3 m/s wind speed may be Bragg scattering, depending on the spectral model used. Even at nadir, a substantial fraction of the backscatter may be described as Bragg scattering at very low wind speeds, depending on the level of wind variability. The figure shows that the conventional wisdom that the transition to Bragg scattering occurs between 10° and 20° incidence angles is not bad but that the transition depends in detail on many factors. The figure illustrates the most important factors, those of wind speed and wave spectrum; the Bragg scattering fraction also depends on azimuth angle and polarization to a lesser degree.

7. Conclusion

[48] This article has presented a new stochastic, multiscale model for microwave backscatter from the sea that is built on recent advances in scattering theories. The model partitions surface waves on the ocean into three different categories depending on their mean square heights and models the scattering from each part by different approximations to the scattering integral given in equation (1). Short and intermediate scales are tilted, advected, and modulated by larger-scale waves. The results show that backscatter seldom arises directly from the large-scale surface. Even at nadir, the scattering can very accurately be viewed as Kirchhoff scattering from tilted intermediate-scale waves. The model explains most features of data collected to date rather accurately, including the level and wind dependence of nadir backscatter and the wind and azimuth angle dependence of 10° backscatter that has recently been reported [*Hesany et al.*, 2000]. Both of these results are obtained without recourse to an ''effective reflection coefficient''.

[49] Some aspects of the model presented here are clearly inadequate. As mentioned in the previous section, the dependence of cross sections on azimuth angle is not sufficiently strong for either of the spectral models considered, indicating that the angular spreading functions of these

Figure 5. (opposite) Predicted cross sections as a function of azimuth angle compared with data collected from an airship by *Plant et al.* [1998]. An azimuth angle of zero indicated an upwind antenna look direction. Highest data and predictions are at a wind speed of 8 m/s; lowest are at 2 m/s. Solid lines predicted by the model using the D spectrum with no wind variability; dotted lines predicted using the D spectrum with the standard deviation of wind speed equal to 1.5 m/s; dashed lines predicted using the E spectrum. Note that no solid line is visible at a 50° incidence angle and a wind speed of 2 m/s because it is below the bottom of the graph.

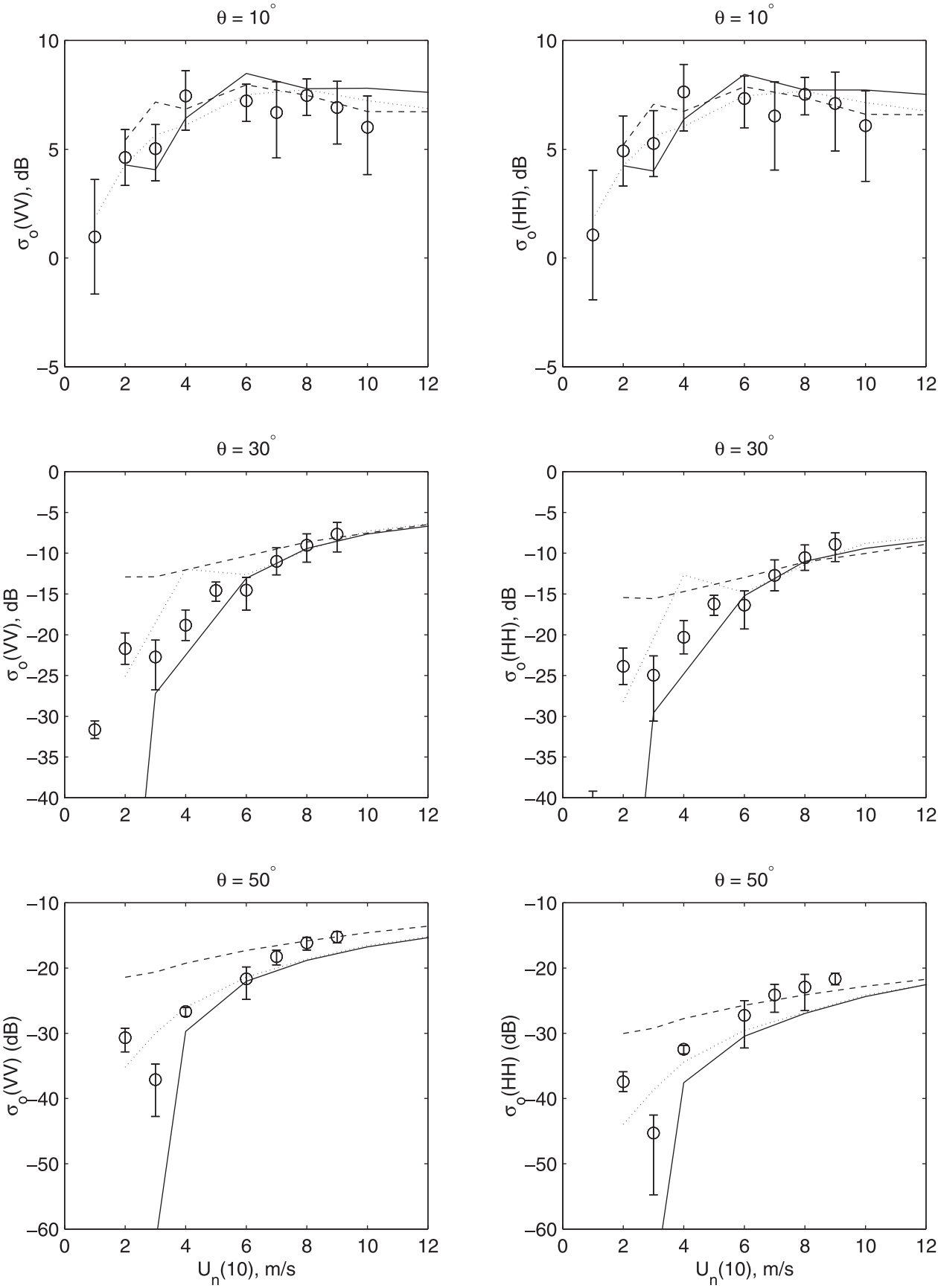

Figure 6. Predicted azimuthally averaged cross sections as a function of wind speed compared with data collected from an airship by *Plant et al.* [1998]. Solid lines - D spectrum with no wind variability; dotted line - D spectrum with the standard deviation of wind speed equal to 1.5 m/s; dashed lines - E spectrum.

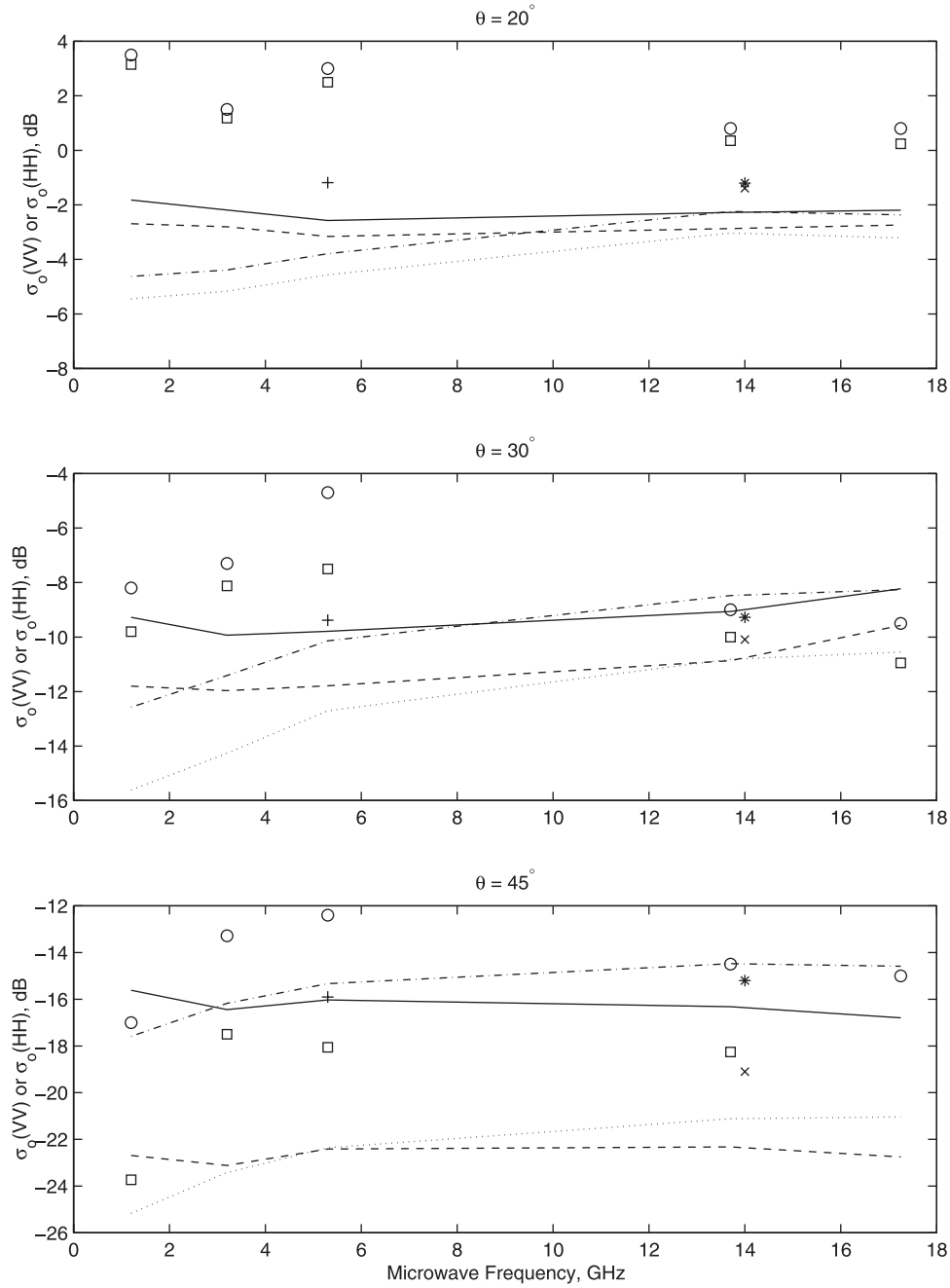

Figure 7. Azimuthally averaged cross sections at various frequencies at a wind speed of 10 m/s. Data from *Unal et al.* [1991] - circles are VV polarization; squares are HH polarization. CMOD4 scatterometer model function - plus at VV polarization. NSCAT2 model function - asterisk at VV polarization, x at HH polarization. Predictions of the model: using D spectrum, solid lines are VV polarization, dashed lines are HH polarization; using E spectrum, dash-dotted lines are VV polarization, dotted lines are HH polarization.

spectral models may not sufficiently anisotropic at high wave numbers. Also, upwind/downwind ratio are not always predicted accurately. This is clearly a result of using a linear model of the modulation of short waves by long. This is especially evident from the fact that the linear modulations produced negative spectral densities if airflow modulation was included. A higher-order model of short wave modulation has recently been published by *Elfouhaily et al.* [2001b]. Inclusion of this or other nonlinear modulating effects in the model may improve upwind/downwind ratios in the future. The underestimation of the HH/VV cross section ratio indicates a further inadequacy in the model. We hope that the future inclusion of bound, tilted wave effects will reduce this problem. Finally, the fact that the division between scales depends on microwave frequency and incidence angle is clearly conceptually inadequate. Since longer scales modulate shorter ones, this, improbably, makes the properties of the sea surface depend-

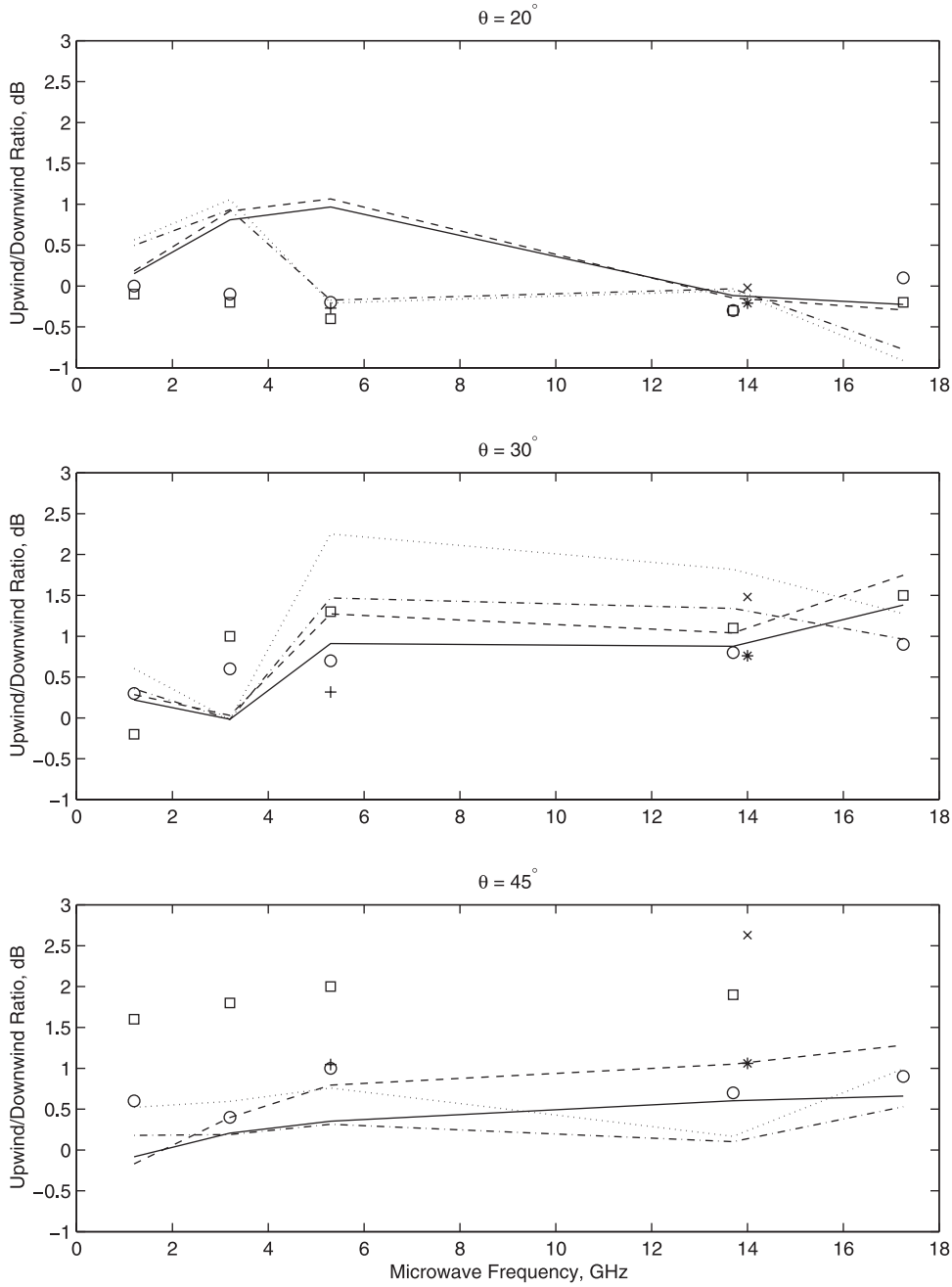

Figure 8. Upwind/Downwind ratios at various frequencies at 10 m/s. Symbols and lines are as in Figure 7.

ent on the microwave system observing it. This is a problem that the present model has in common with other composite-type models, however. As long as the scale separation parameter is not critical, as it is not here, then this problem is probably not too severe.

[50] In the present work, we have concentrated on presenting the model and comparing its predictions using two different spectral models with data collected at incidence angles below 50°. We believe that the model can eventually be made accurate out to incidence angles of about 80° but effects of bound waves [*Plant*, 1997; *Plant et al.*, 1999] will need to be included. We are presently working to develop an understanding of these waves for use in this extension. This model also has the potential to predict Doppler spectra as a function of time and space at any incidence angle out to 80°. Our future work will also focus on this extension.

Appendix A

[51] In this appendix, we show that the scattering theories of *Fung et al.* [1992], hereafter FLC, and of *Voronovich* [1994], hereafter Voronovich, yield identical results for the normalized radar cross section of the sea for backscatter for incidence angles above which multiple scattering is important. Voronovich sets this limit at 90° minus the RMS slope of the surface. As mentioned in the text, this is not the case for bistatic scattering where the Integral Expansion Method of FLC does not seem to be correct [*Elfouhaily et al.*, 2001a].

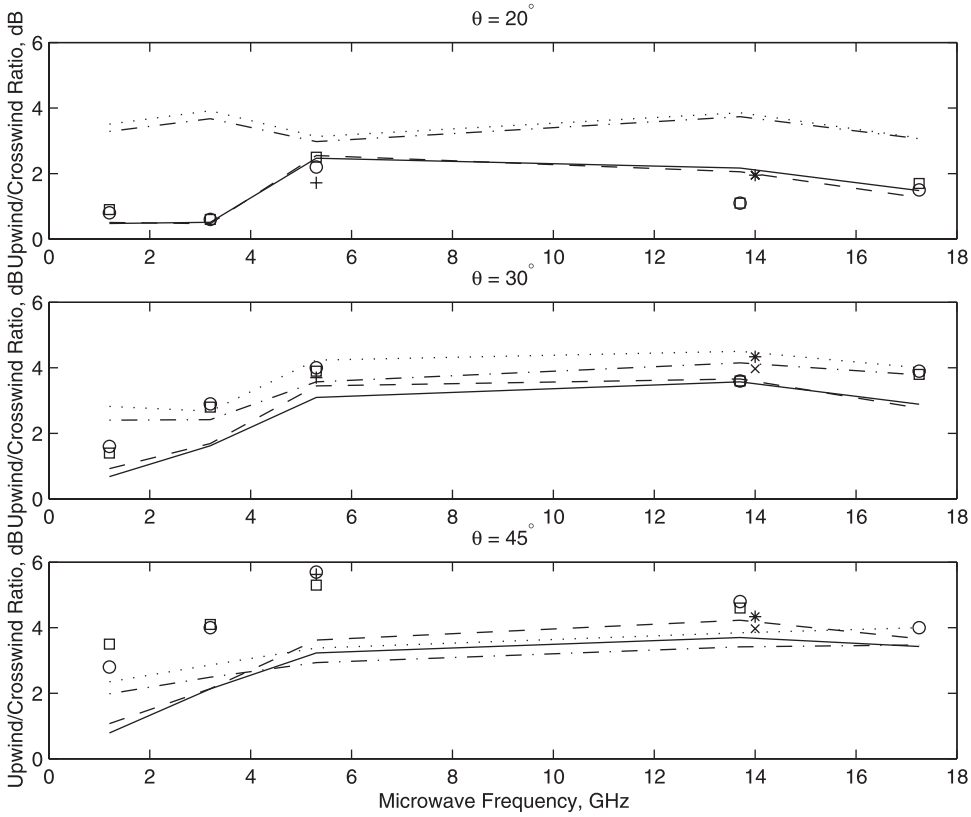

Figure 9. Upwind/Crosswind ratios at various frequencies at a wind speed of 10 m/s. Symbols and lines are as in Figure 7.

We consider first the Integral Expansion Method and then turn to the Small Slope Approximation of Voronovich.

A1. Integral Expansion Method

[52] In their equation (77) FLC give their backscattering cross section for the polarizations p and q as the sum of three terms:

$$\sigma^o_{qp} = \sigma^k_{qp} + \sigma^{kc}_{qp} + \sigma^e_{qp} \tag{A1}$$

The terms on the right hand side are given in their equations (78), (79), and (80). These equations involve the parameters of integration u and v. They show, however, that their

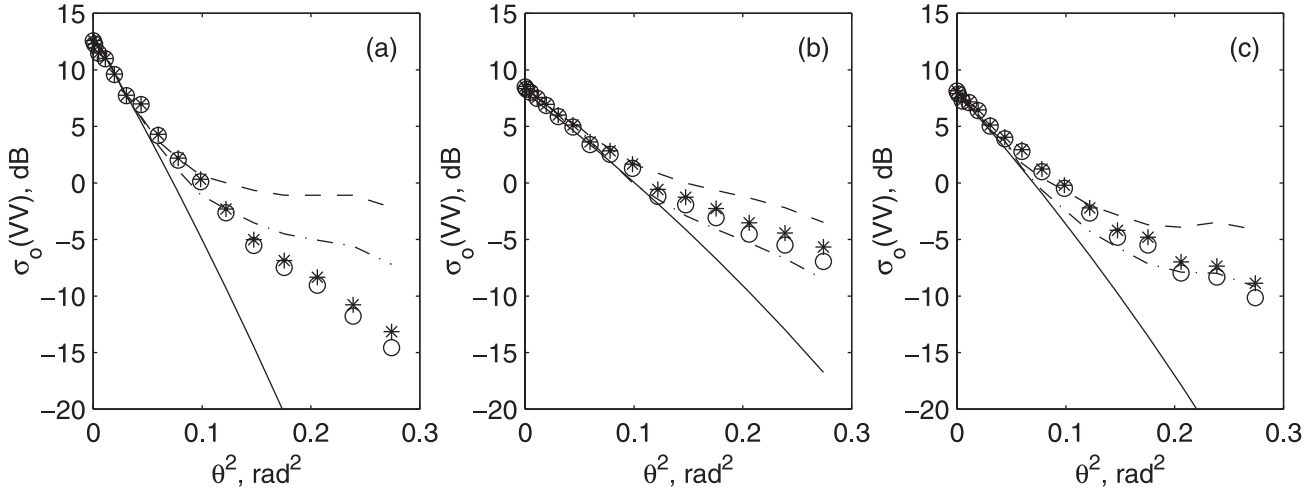

Figure 10. Normalized radar cross section at 36 GHz versus incidence angle squared. Data have been fit to the model at nadir. Asterisks and circles are predictions of the present model for VV and HH polarizations, respectively, using the D spectrum. The solid line is $\tan^2\theta$ as given by the quasi-specular model. Dashed lines are $\ln(P_r)$ given by *Banner et al.* [1999] divided by 0.23. Dash-dotted lines are these data corrected for illuminated area and range. (a) Upwind/downwind antenna look, wind speed = 6.8 m/s. (b) Upwind/downwind antenna look, wind speed = 15.4 m/s. (c) Cross-wind antenna look, wind speed = 15.4 m/s.

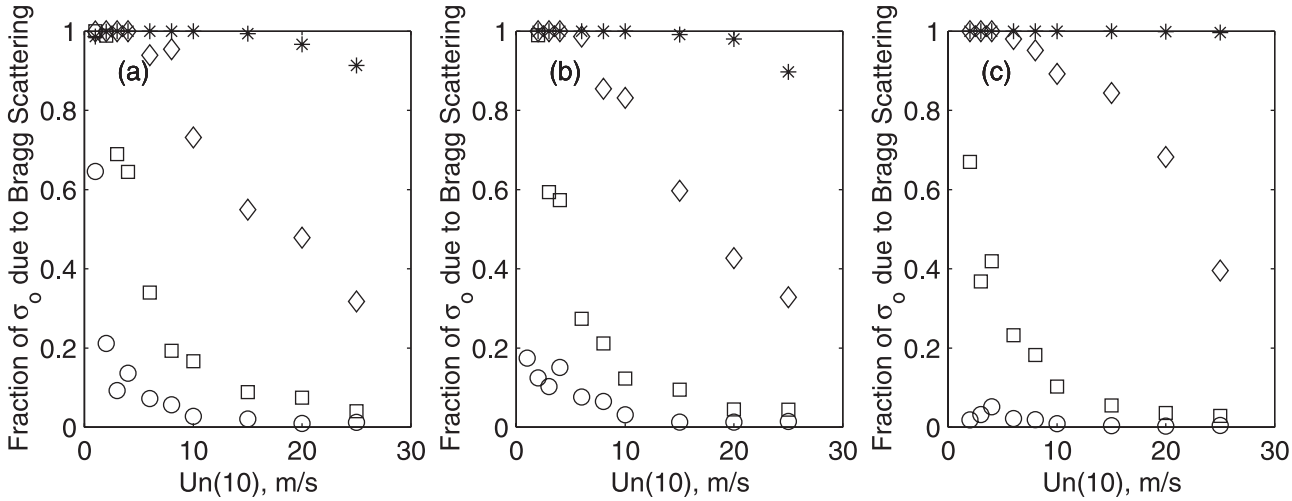

Figure 11. Fraction of azimuthally averaged, VV polarization cross section due to Bragg scattering versus wind speed. Circles - 0° incidence, squares - 10° incidence, diamonds - 20° incidence, asterisks - 30° incidence. (a) D spectrum with no wind variability, (b) D spectrum with the standard deviation of wind speed equal to 1.5 m/s, and (c) E spectrum.

equations include both single and multiple scattering and we expect that the multiple scattering effects will be small for all but the highest incidence angles. They also show that one function in their integrands, $F_{qp}(u, v)$, appears in the single scattering equations for small wave heights or low frequencies, ie, for $k_o \cos\theta\sigma < 3$, only with $v = 0$ and $u = \pm k_o \sin\theta$. We may therefore include all of their small wave height and low frequency single scatter terms in the equations if we set $F_{qp}(u, v) = [F_{qp}(k_o \sin\theta, 0) + (F_{qp}(-k_o \sin\theta, 0)]/2$ in their equations. This procedure also leaves some multiple scattering terms in the equations but we make the assumption that they are very small compared to the single scattering ones in our region of interest. We now consider the terms on the right side of equation (A1) after correcting some small typos in the equations of FLC.

[53] Equation (78) does not involve $F_{qp}(u, v)$ so we may take it as it stands. Letting $k_x = k_o \sin\theta$ and $k_z = k_o \cos\theta$, we have:

$$\sigma_{qp}^{k} = \frac{k_o^2}{4\pi} |f_{qp}|^2 \, e^{-4k_z^2\sigma^2} \int \left(e^{4k_z^2\sigma^2\rho(\xi,\zeta)} - 1\right) e^{-i2k_x\xi} d\xi d\zeta. \quad \text{(A2)}$$

FLC give expressions for f_{qp}, which we will consider later.

[54] Making our substitution for $F_{qp}(u, v)$ in equation (79) and integrating over u and v yields,

$$\sigma_{qp}^{k_c} = \frac{k_o^2}{8\pi} Re\{[F_{qp}(k_x, 0) + F_{qp}(-k_x, 0)] f_{qp}^*\} \int e^{-3k_z^2\sigma^2} e^{-k_z^2\sigma^2\rho(\xi-\xi',\zeta-\zeta')} \cdot \left(e^{2k_z^2\sigma^2[\rho(\xi,\zeta)+\rho(\xi',\zeta')]} - 1\right) \delta(\xi - \xi')\delta(\zeta - \zeta') e^{-jk_x(\xi+\xi')} d\xi d\zeta d\xi' d\zeta \quad \text{(A3)}$$

Carrying out the ξ' and ζ' integrals and the "Re" operation yields,

$$\sigma_{qp}^{k_c} = \frac{k_o^2}{16\pi} \left([F_{qp}(k_x, 0) + F_{qp}(-k_x, 0)] f_{qp}^* + [F_{qp}^*(k_x, 0) + F_{qp}^*(-k_x, 0)] f_{qp}\right) e^{-4k_z^2\sigma^2} \int \left(e^{-4k_z^2\sigma^2\rho(\xi,\zeta)} - 1\right) e^{-i2k_x\xi} d\xi d\zeta \quad \text{(A4)}$$

This is the same as equation (78) if we let

$$|f_{qp}|^2 \rightarrow \left([F_{qp}(k_x, 0) + (F_{qp}(-k_x, 0)] f_{qp}^* + [F_{qp}^*(k_x, 0) + F_{qp}^*(-k_x, 0)] f_{qp}\right)/4. \quad \text{(A5)}$$

[55] Turning now to equation (80), after our substitution for $F_{qp}(u, v)$, we can carry out the integrals over u, v, u′, and v′ to obtain

$$\sigma_{qp}^{c} = \frac{k_o^2}{64\pi} |F_{qp}(k_x, 0) + F_{qp}^*(-k_x, 0)|^2 \int e^{-2k_z^2\sigma^2} e^{-k_z^2\sigma^2[\rho(\tau+\xi-\xi',\kappa+\zeta-\zeta')+\rho(\tau,\kappa)]} \cdot \left(e^{k_z^2\sigma^2[\rho(\xi+\tau,\kappa+\zeta)+\rho(\xi'-\tau,\zeta'-\kappa)+\rho(\xi,\zeta+)+\rho(\xi',\zeta')]} - 1\right) \cdot \delta(\kappa)\delta(\tau)\delta(\zeta - \zeta' + \kappa)\delta(\xi - \xi' + \tau) \cdot e^{-i2k_x(\xi+\xi')} d\xi d\zeta d\xi' d\zeta' d\tau d\kappa \quad \text{(A6)}$$

Then carrying out the κ, τ, ς′, and ζ′ yields,

$$\sigma_{qp}^{c} = \frac{k_o^2}{64\pi} |F_{qp}(k_x, 0) + F_{qp}^*(-k_x, 0)|^2 \, e^{-4k_z^2\sigma^2} \int \left(e^{4k_z^2\sigma^2\rho(\xi,\zeta)} - 1\right) e^{-i2k_x\xi} d\xi d\zeta \quad \text{(A7)}$$

This is once again the same as equation (78) with the substitution

$$|f_{qp}|^2 \rightarrow |F_{qp}(k_x, 0) + F_{qp}^*(-k_x, 0)|^2 / 16 \quad \text{(A8)}$$

Table 1. Mean Square Slopes, Measured and Modeled

	S_u		S_c	
Wind Speed, m/s	*Banner et al.* [1999]	Present	*Banner et al.* [1999]	Present
6.8	0.013	0.015	0.009	0.012
15.4	0.029	0.031	0.020	0.026

[56] We may therefore write the result of the Integral Expansion Method for the case of backscatter at incidence angles that are not too large to be

$$\sigma^o_{qp} = \frac{k_o^2}{4\pi} |\Gamma_{qp}|^2 \, e^{-4k_z^2\sigma^2} \int \left(e^{4k_z^2\sigma^2\rho(\xi,\zeta)} - 1\right) e^{-i2k_x\xi} d\xi d\zeta \quad \text{(A9)}$$

where

$$\Gamma_{qp} = f_{qp} + [F_{qp}(k_x, 0) + F_{qp}(-k_x, 0)]/4 \quad \text{(A10)}$$

[57] For vertical polarization on both transmission and reception, $q = p = v$ and FLC show that if the permeability of seawater is one,

$$\Gamma_{vv} = \frac{2R_v}{\cos\theta} + \left(\frac{\sin^2\theta(1+R_v)^2}{2\cos\theta}\right)\left(1 - \frac{1}{\epsilon} + \frac{\sin^2\theta(\epsilon-1)}{\epsilon^2\cos^2\theta}\right) \quad \text{(A11)}$$

where ϵ is the relative dielectric constant and R_v is the Fresnel reflection coefficient for vertical polarization

$$R_v = \frac{\epsilon^2\cos^2\theta - \epsilon - \sin^2\theta}{[\epsilon\cos\theta + \sqrt{\epsilon - \sin^2\theta}]^2}. \quad \text{(A12)}$$

In their Section VII, FLC. go on to show that B_{vv} may be written in the form

$$\Gamma_{vv} = R_v\cos^2\theta + \frac{\sin^2\theta(1+R_v)^2}{2}\left(1 - \frac{1}{\epsilon}\right) \quad \text{(A13)}$$

Substituting for R_v yields,

$$\Gamma_{vv} = \frac{2}{\cos\theta}\left[\frac{2(\epsilon-1)[\epsilon(1+\sin^2\theta) - \sin^2\theta]\cos\theta}{\left[\epsilon\cos\theta + \sqrt{\epsilon - \sin^2\theta}\right]^2}\right] \quad \text{(A14)}$$

Thus we may write,

$$\sigma^o_{vv} = \frac{k_o^2}{\pi\cos^2\theta} |g_{vv}|^2 \, e^{-4k_z^2\sigma^2} \int \left(e^{4k_z^2\sigma^2\rho(\xi,\zeta)} - 1\right) e^{-i2k_x\xi} d\xi d\zeta \quad \text{(A15)}$$

where

$$g_{vv} = \frac{(\epsilon-1)[\epsilon(1+\sin^2\theta) - \sin^2\theta]\cos^2\theta}{\left[\epsilon\cos\theta + \sqrt{\epsilon - \sin^2\theta}\right]^2} \quad \text{(A16)}$$

[58] Similarly, for horizontal polarization, FLC give

$$\Gamma_{hh} = -\frac{2R_h}{\cos\theta} - \left(\frac{\sin^2\theta(1+R_h)^2}{2\cos\theta}\right)\left(\frac{\epsilon-1}{\cos^2\theta}\right) \quad \text{(A17)}$$

where the Fresnel reflection coefficient for horizontal polarization is

$$R_h = \frac{1-\epsilon}{[\cos\theta + \sqrt{\epsilon - \sin^2\theta}]^2}. \quad \text{(A18)}$$

Some straightforward algebra shows that we may write Γ_{hh} as

$$\Gamma_{hh} = -2R_h\cos\theta \quad \text{(A19)}$$

or, substituting R_h,

$$\Gamma_{hh} = \frac{2(\epsilon-1)\cos\theta}{\left[\cos\theta + \sqrt{\epsilon - \sin^2\theta}\right]^2} \quad \text{(A20)}$$

Thus we may write

$$\sigma^o_{hh} = \frac{k^2}{\pi\cos^2\theta} |g_{hh}|^2 \, e^{-4k_z^2\sigma^2} \int \left(e^{4k_z^2\sigma^2\rho(\xi,\zeta)} - 1\right) e^{-i2k_x\xi} d\xi d\zeta \quad \text{(A21)}$$

where

$$g_{hh} = \frac{(\epsilon-1)\cos^2\theta}{\left[\cos\theta + \sqrt{\epsilon - \sin^2\theta}\right]^2} \quad \text{(A22)}$$

A2. Small Slope Approximation

[59] In his equation 6.9, Voronovich gives,

$$\sigma^{NN_0}_{\alpha\alpha_o} = (2q_k^{(N)}q_{k_o}^{(N_o)})^2 \, |B^{NN_o}_{\alpha\alpha_o}(\vec{k}, \vec{k}_o)|^2 \int e^{-(\vec{k}-\vec{k}_o)\cdot\vec{r}} \, e^{-Q^2\sigma^2} \cdot \left(\frac{\exp(Q^2W(\vec{r})) - 1}{Q^2}\right) \frac{d\vec{r}}{(2\pi)^2} \quad \text{(A23)}$$

This is the first-order expression for the incoherent part of the scattering cross section given by the small slope approximation. In this notation, N and N_o are superscripts indicating the medium; we take 1 to be air, 2 to be water. We are interested in $N = N_o = 1$ for backscatter in air. The letters α and α_o indicate polarization and in Voronovich's notation, 1 is vertical and 2 is horizontal. We will use q, p, v and h, though, to agree with the notation of FLC. Then $\sigma^{11}_{\alpha\alpha o}$ becomes σ^o_{qp}. In equation (A23), $\vec{k}$ and $\vec{k}_o$ are horizontal component of the scattered and incident radiation, respectively. For backscatter, $\vec{k}_o = -\vec{k} \equiv (k_x, k_y)$. The quantities $q_k^{(N)}$ and $q_{ko}^{(No)}$ are vertical wave numbers of scattered and incident waves and, in general, can be complex. For backscatter, we have,

$$q_{k_o}^{(1)} = q_k^{(1)} = k_o\cos\theta \equiv k_z \quad \text{(A24)}$$

Both q_{ko} and q_k are positive because by Voronovich's definition they are in the first quadrant of the complex plane. Q is given by

$$Q = -q_k^{(1)} - q_{k_o}^{(1)} = -2k_o\cos\theta \equiv -2k_z \quad \text{(A25)}$$

$W(r)$ is the coherence function, $\sigma^2\rho$, in the notation of FLC. Letting $\vec{r} = (\zeta, \xi)$ in equation (A23), we have

$$\sigma^o_{qp} = \left(\frac{k_z^2}{(2\pi)^2}\right) |B_{qp}|^2 \, e^{-4k_z^2\sigma^2} \int \left(e^{4k_z^2\sigma^2\rho(\zeta,\xi)} - 1\right) e^{-i2k_x\xi} d\zeta d\xi. \quad \text{(A26)}$$

We omit the dependence of B_{qp} on $\vec{k}$ and $\vec{k}_o$ because we will show shortly that this dependence does not exist for backscatter. Equation (A26) has the same form as the result of FLC; we now proceed to show that B_{qp} is such that the two results are, in fact, identical.

[60] In equation (4.15), Voronovich gives,

$$B_{\alpha\alpha_o} = d_{1\alpha}^{(1)}(k)\left(\frac{\vec{k}\cdot\vec{k}_o}{kk_o}(\hat{\sigma}_3)_{\alpha\alpha_o} + \frac{\vec{N}\cdot\vec{k}\times\vec{k}_o}{kk_o}(\hat{\sigma}_1)_{\alpha\alpha_o} - \frac{1}{\epsilon_1\epsilon_2}d_{2\alpha}^{(1)}(k)\frac{1}{2}(\hat{\sigma}_o+\hat{\sigma}_3)_{\alpha\alpha_o}d_{2\alpha_o}^{(1)}(k_o)\right)d_{1\alpha_o}^{(1)}(k_o) \quad \text{(A27)}$$

In his equation (3.5), Voronovich shows that

$$(\hat{\sigma}_3)_{11} = 1, (\hat{\sigma}_3)_{22} = -1, (\hat{\sigma}_o)_{11} = 1, (\hat{\sigma}_o)_{22} = 1 \quad \text{(A28)}$$

Because $q_k^{(2)} = \sqrt{\epsilon_2}k\cos\theta_w$, where $\cos\theta_w$ is the incidence angle in water, the set of equations after Voronovich's equation (4.14) yield,

$$d_{11}^{(1)}(k) = \frac{k\cos\theta_w\sqrt{\epsilon_1\epsilon_2(\epsilon_2-\epsilon_1)}}{(\epsilon_2 k\cos\theta + \epsilon_1\sqrt{\epsilon_2}k\cos\theta_w)} \quad \text{(A29)}$$

$$d_{12}^{(1)}(k) = \frac{k\sqrt{(\epsilon_2-\epsilon_1)}}{(k\cos\theta + \sqrt{\epsilon_2}k\cos\theta_w)} \quad \text{(A30)}$$

$$d_{21}^{(1)}(k) = \frac{\epsilon_2 k\sin\theta}{\sqrt{\epsilon_2}k\cos\theta_w} \quad \text{(A31)}$$

$$d_{22}^{(1)}(k) = 0 \quad \text{(A32)}$$

Here $\epsilon_1(=1)$ is the permittivity of air, and ϵ_2 ($\equiv\epsilon$) is the permittivity of water.

[61] Note that k cancels out in all equations for d's. Also note that

$$\frac{\vec{k}\cdot\vec{k}_o}{kk_o} = -1 \quad \text{(A33)}$$

and

$$\vec{k}\times\vec{k}_o = 0 \quad \text{(A34)}$$

for backscatter. Finally, Snell's law is

$$\sin\theta = \sqrt{\epsilon}\sin\theta_w. \quad \text{(A35)}$$

This implies that

$$\cos\theta_w = \sqrt{1-\frac{1}{\epsilon}\sin^2\theta} \quad \text{(A36)}$$

[62] Then, substituting all of this in equation (A27) and converting to the notation of FLC, we have,

$$B_{vv} = \frac{(\epsilon-1)[\sin^2\theta - \epsilon(1+\sin^2\theta)]}{\left[\epsilon\cos\theta + \sqrt{\epsilon - \sin^2\theta}\right]^2} \quad \text{(A37)}$$

for VV polarization and

$$B_{hh} = \frac{\epsilon-1}{\left[\cos\theta + \sqrt{\epsilon-\sin^2\theta}\right]^2} \quad \text{(A38)}$$

for HH polarization. When these expressions for B_{vv} and B_{hh} are inserted into equation (A26), they yield precisely the results of FLC expressed in equations (A15) and (A21) divided by 4π. This is because Voronovich uses a definition of cross section more common in the US in acoustics and it differs from the standard US microwave usage by precisely this factor of 4π [*Dahl et al.*, 1997].

Appendix B

[63] Consider a antenna transmitting a beam directed at a perfectly flat water surface at a very small incidence angle, θ. The radar equation tells us that the power received by this antenna due to backscatter from the surface is

$$P_r = \frac{P_t G_o^2\lambda^2\sigma_o(\theta)A_s}{(4\pi)^3 R_o^4} \quad \text{(B1)}$$

where P_t is the transmitted power, G_o is the maximum gain of the antenna, λ is the microwavelength, A_s is the two-way illuminated surface area, and R_o is the range to the surface. A_s is given by

$$A_s = \pi R^2(\Phi_2/2)^2 = \frac{\pi}{8}R^2\Phi_1^2 \quad \text{(B2)}$$

where Φ_1 and Φ_2 are one and two-way, full, half-power beam widths, respectively.

[64] Now the power scattered from the surface will exactly correspond to the power that would be transmitted by an image of the antenna below the surface, reduced by the square of the reflection coefficient, R. Thus, another way to write P_r is

$$P_r = \frac{P_t\,|R(0)|^2\,G(\theta)A_e}{4\pi(2R)^2} \quad \text{(B3)}$$

where A_e is the effective antenna pattern given by

$$A_e = \frac{\lambda^2 G(\theta)}{4\pi} \quad \text{(B4)}$$

[65] Thus, equating the received powers from the two expressions and solving for σ_o, we get

$$\sigma_o = \left(\frac{8\,|R(0)|^2}{\Phi_1^2}\right)\left(\frac{G^2(\theta)}{G_o^2}\right) \quad \text{(B5)}$$

The ratio of the gain of the antenna in a particular direction to the maximum gain will depend on the antenna. However, we may approximate it for a Gaussian beam width by an exponential function whose full, half-power beam width is determined by Φ_2. Then we get

$$\sigma_o = \left(\frac{8\,|R(0)|^2}{\Phi_1^2}\right)e^{-8(\ln 2)\theta^2/\Phi_1^2}. \quad \text{(B6)}$$

[66] **Acknowledgments.** The author is grateful to Peter Dahl for once again interesting him in physically based scattering models. Discussions with Alexander Voronovich, Don Thompson, and Tony Elfouhaily have also been most helpful. This work was sponsored by the Space and Remote Sensing Program of the Office of Naval Research under grant number N00014-00-1-0075.

References

Apel, J. R., An improved model of the ocean surface wave vector spectrum and its effects on radar backscatter, *J. Geophys. Res.*, *99*, 16,269–16,291, 1994.

Banner, M. L., Equilibrium spectra of wind waves, *J. Phys. Oceanogr.*, *20*, 966–984, 1990.

Banner, M. L., W. Chen, E. J. Walsh, J. B. Jensen, S. Lee, and C. Fandry, The Southern Ocean Waves Experiment, part I, Overview and mean results, *J. Phys. Oceanogr.*, *29*, 2130–2145, 1999.

Barrick, D. E., Rough surface scattering based on the specular point theory, *IEEE Trans. Antennas Propag.*, *16*, 449–454, 1968.

Bass, F. G., I. M. Fuks, A. I. Kalmykov, I. E. Ostrovsky, and A. D. Rosenberg, Very high frequency radiowave scattering by a disturbed sea surface, part II, Scattering from an acutal sea surface, *IEEE Trans. Antennas Propag.*, *AP-16*, 560–568, 1968.

Beckmann, P., and A. Spizzichino, *The Scattering of Electromagnetic Waves from Rough Surfaces*, Pergamon, New York, 1963.

Colton, M. C., W. J. Plant, W. C. Keller, and G. L. Geernaert, Tower-based measurements of normalized radar cross section from Lake Ontario: Evidence of wind stress dependence, *J. Geophys. Res.*, *100*, 8791–8813, 1995.

Dahl, P. H., W. J. Plant, B. Nützel, A. Schmidt, H. Herwig, and E. A. Terray, Simultaneous acoustic and microwave backscattering from the sea surface, *J. Acoust. Soc. Am.*, *101*, 2583–2595, 1997.

Donelan, M. A., The dependence of the aerodynamic drag coefficient on wave parameters, paper presented at First International Conference on Meteorology and Air-Sea Interaction of the Coastal Zone, Am. Meteorol. Soc., Boston, Mass., 1982.

Donelan, M. A., and W. J. Pierson Jr., Radar scattering and equilibrium ranges in wind-generated waves with application to scatterometry, *J. Geophys. Res.*, *92*, 4971–5030, 1987.

Donelan, M. A., J. Hamilton, and W. H. Hui, Directional spectra of wind-generated waves, *Philos. Trans. R. Soc. London, Ser. A*, *315*, 509–562, 1985.

Durden, S. L., and J. F. Vesecky, A physical radar cross-section model for a wind-driven sea with swell, *IEEE J. Oceanic Eng.*, *OE-10*, 445–451, 1985.

Elfouhaily, T., B. Chapron, K. Katsaros, and D. Vandemark, A unified directional spectrum for long and short wind-driven waves, *J. Geophys. Res.*, *102*, 15,781–15,796, 1997.

Elfouhaily, T., D. R. Thompson, D. E. Freund, D. Vandemark, and B. Chapron, A new bistatic model for electromagnetic scattering from perfectly conducting random surfaces: Numerical evaluation and comparison with SPM, *Waves Random Media*, *11*, 33–43, 2001a.

Elfouhaily, T., D. R. Thompson, D. Vandemark, and B. Chapron, Higher-order hydrodynamic modulation: Theory and applications for ocean waves, *Proc. R. Soc. London, Ser. A*, *457*, 1–24, 2001b.

Fung, A. K., Z. Li, and K. S. Chen, Backscattering from a randomly rough dielectric surface, *IEEE Trans Geosci. Remote Sens.*, *30*, 356–369, 1992.

Hara, T., and W. J. Plant, Hydrodynamic modulation of short wind-wave spectra by long waves and its measurement using microwave backscatter, *J. Geophys. Res.*, *99*, 9767–9784, 1994.

Hesany, V., W. J. Plant, and W. C. Keller, The normalized radar cross section of the sea at 10° incidence, *IEEE Trans. Geosci. Remote Sens.*, *38*, 64–72, 2000.

Holliday, D., Resolution of a controversy surrounding the Kirchhoff approach and the small perturbation method in rough surface scattering theory, *IEEE Trans. Antennas Propag.*, *AP-35*, 120–122, 1987.

Hwang, P. A., W. J. Teague, G. A. Jacobs, and D. W. Wang, A statistical comparison of wind speed, wave height, and wave period derived from satellite altimeters and ocean buoys in the Gulf of Mexico region, *J. Geophys. Res.*, *103*, 10,451–10,468, 1998.

Keller, M. R., W. C. Keller, and W. J. Plant, A wave tank study of the dependence of X band cross sections on wind speed and water temperature, *J. Geophys. Res.*, *97*, 5771–5792, 1992.

Longuet-Higgins, M. S., D. E. Cartwright, and N. D. Smith, Observations of the directional spectrum of sea waves using the motions of a floating buoy, in *Ocean Wave Spectra*, pp. 111–136, Prentice-Hall, Old Tappan, N.J., 1963.

Plant, W. J., On the steady-state energy balance of short gravity wave systems, *J. Phys. Oceanogr.*, *10*, 1340–1352, 1980.

Plant, W. J., A relationship between wind stress and wave slope, *J. Geophys. Res.*, *87*, 1961–1967, 1982.

Plant, W. J., A two-scale model of short wind generated waves and scatterometry, *J. Geophys. Res.*, *91*, 10,735–10,749, 1986.

Plant, W. J., Bragg scattering of electromagnetic waves from the air/sea interface, in *Surface Waves and Fluxes*, vol. II, *Remote Sensing*, edited by G. L. Geernaert and W. J. Plant, pp. 41–108, Kluwer Acad., Norwell, Mass., 1990.

Plant, W. J., A model for microwave Doppler sea return at high incidence angles: Bragg scattering from bound, tilted waves, *J. Geophys. Res.*, *109*, 21,131–21,146, 1997.

Plant, W. J., Effects of wind variability on scatterometry at low wind speeds, *J. Geophys. Res.*, *105*, 16,899–16,910, 2000.

Plant, W. J., and J. W. Wright, Phase speeds of upwind and downwind traveling short gravity waves, *J. Geophys. Res.*, *85*, 3304–3310, 1980.

Plant, W. J., W. C. Keller, V. Hesany, and K. Hayes, Measurements of the marine boundary layer from an airship, *J. Atmos. Oceanic Technol.*, *15*, 1433–1458, 1998.

Plant, W. J., W. C. Keller, V. Hesany, T. Hara, E. Bock, and M. Donelan, Bound waves and Bragg scattering in a wind wavetank, *J. Geophys. Res.*, *104*, 3243–3263, 1999a.

Plant, W. J., P. H. Dahl, and W. C. Keller, Microwave and acoustic scattering from parasitic capillary waves, *J. Geophys. Res.*, *104*, 25,853–25,866, 1999b.

Romeiser, R., W. Alpers, and V. Wismann, An improved composite surface model for the radar backscattering cross section of the ocean surface, 1, Theory of the model and optimization/validation by scatterometer data, *J. Geophys. Res*, *102*, 25,237–25,250, 1997.

Thorsos, E. I., and S. L. Broschat, An investigation of the small slope approximation for scattering from rough surfaces, part I, Theory, *J. Acoust. Soc. Am.*, *97*, 2082–2093, 1995.

Ulaby, F. T., R. K. Moore, and A. K. Fung, *Microwave Remote Sensing*, vol. II, 935 pp., Artech House, Norwood, Mass., 1982.

Unal, C. M. H., P. Snoeij, and P. J. F. Swart, The polarization-dependent relation between radar backscatter from the ocean surface and surface wind vector at frequencies between 1 and 18 GHz, *IEEE Trans. Geosci. Remote Sens.*, *29*, 621–626, 1991.

Valenzuela, G. R., Scattering of electromagnetic waves from a tilted slightly rough surface, *Radio Sci.*, *3*, 1057–1066, 1968.

Valenzuela, G. R., Theories for the interaction of electromagnetic and ocean waves—A review, *Boundary Layer Meteorol.*, *13*, 61–85, 1978.

Voronovich, A. G., Small-slope approximation in wave scattering by rough surfaces, *Sov. Phys. JETP, Engl. Transl.*, *62*, 65–70, 1985.

Voronovich, A. G., Small-slope approximation for electromagnetic wave scattering at the rough interface of two dielectric half-spaces, *Waves Random Media*, *4*, 337–367, 1994.

Voronovich, A. G., A two-scale model from the point of view of the small-slope approximation, *Waves Random Media*, *6*, 73–83, 1996.

Walsh, E. J., D. C. Wandemark, C. A. Friehe, S. P. Burns, D. Khelif, R. N. Swift, and J. F. Scott, Measuring sea surface mean square slope with a 36-GHz scanning radar altimeter, *J. Geophys. Res*, *103*, 12,587–12,601, 1998.

Wright, J. W., Backscattering from capillary waves with application to sea clutter, *IEEE Trans. Antennas Propagl*, *AP-14*, 749, 1966.

Wright, J. W., A new model for sea clutter, *IEEE Trans. Antennas Propag.*, *AP-16*, 217–223, 1968.

W. J. Plant, Applied Physics Laboratory, University of Washington, Seattle, WA 98105-6698, USA. (plant@apl.washington.edu)